VARIABLE-SPEED, ROBUST SYN-CHRONOUS RELUCTANCE MACHINE DRIVE SYSTEMS

AALBORG UNIVERSITY
DENMARK

Project title: Variabel hastighed, robust synkron reluctance motor drev systemer
Project data: Journalnr.: 464-11,
                    project nr.: 344-068
Auditor: Assoc. Professor Kaiyuan Lu; Ph. D. student Dong Wang
Address: Aalborg University, Department of Energy Technology, Pontoppidanstraede 101,
                    room 39, DK-9220 Aalborg East

ABSTRACT

The synchronous reluctance (SynRel) machine is getting more and more interests from the industry, since it can provide higher energy efficiency than traditional induction machine at similar production cost. It is a good candidate for super premium efficiency machine and commercial products are available now in the market. The research work in this project aims at developing a simple, compact and robust synchronous reluctance machine drive system that can maximize the performance of the drive at various working conditions.

In this project, the full sensorless synchronous reluctance machine drive system has been extensively tested. Performances achieved in this project have met the original expectations, i.e. the full sensorless drive can operate stably at different speed and load conditions; active damping techniques have been successfully applied to the small-dc link drive with improved drive performances.

Field oriented control assisted with various position estimation algorithms is investigated first in this project. Position sensing via machine flux linkage based on the widely used flux observer is implemented. Experiments show that this popular method may not always work properly and system oscillation will occur when there is a failure in the flux observer. Two solutions from both flux observer enhancement and system frequency response point of views are proposed and verified experimentally. One solution is to enhance the closed-loop observer with a PR controller. The other solution is to damp the oscillation by varying the PI parameters of the speed and current regulators according to the speed estimation error. The former solution can work very well during the steady-state conditions while the other solution is preferred when handling sudden speed changes due to e.g. step load on or off.

As another core part of this project, active damping for small dc-link drive using film capacitor has been extensively studied in this project. In recent years, there is an increasing trend to replace the electrolytic capacitor in the frequency converter with film capacitor, which has a longer service lifetime and no explosion risk. Furthermore, it is possible to achieve a compact converter design by using film capacitor, since the capacitance needed is less due to its high-current-ripple-tolerant capability. This is known as small dc-link drive system. It is shown that the reduced dc-link capacitance of the small dc-link drive may result in dc-link voltage oscillation, which is harmful to the drive system and will reduce the service lifetime. In addtion, the grid current with amplified high order harmonics may fail to meet the requirements of grid standards/regulations. Therefore, techniques to stabilize the dc-link voltage are required. These methods are known as active damping techniques.

Various active damping methods to stabilize the dc-link voltage are investigated in this project. The essential idea and technique details to implement active damping control are thoroughly discussed. Control strategies, which are of great practical values such as minimized system current stress control and optimized voltage utilization control, are discussed as well. The existing active damping methods are often based on signal injection that requires on-line calculation of the compensation gain factors, which are system parameter and operating condition dependent. Thus, a new damping method known as "virtual positive impedance" active damping method is proposed. This method can ensure the system stability without the knowledge of the system parameters and is op-

erating condition independent. A simple compensation gain factor may be introduced when applying the 'virtual positive imdedance' active damping method, which can easily control the level of the damping effects according to different system performance requrements. This method improves the existing active damping techniques and is verified experimentally.

Finally, in this project, the preferred flux linkage based position sensorless control with adaptive PI controllers is used and cooperated with different active damping control methods to drive the small dc-link SynRel machine drive system. The possible interaction between sensorless control and active damping control is investigated, and the solution to achieve a simple and robust variable-speed SynRel machine drive system is proposed. The experimental results show that the introduction of the small dc-link and active damping control algorithms brings very little impact to the performance of the position-sensorless drive. The influence at steady state conditions is negligible. Generally, the system can operate satisfactorily and is robust enough to meet different operation conditions.

In the following sections of this report, first the background and project objectives are given. The detailed information regarding implementation of the small dc-link SynRel machine drive system is presented afterwards. Position sensorless control method and achieved results are given next. Analysis of the small dc-link system is then introduced to cover the important fundamentals in understanding small dc-link drive system stability issues. This is followed by the presentation of active damping methods implemented in this project. Full sensorless operation of this small dc-link Syn-Rel machine drive system is demonstrated at the end. Finally, conclusion and suggestions for future work is summerized.

1   PROJECT INTRODUCTION

1.1   Background

Energy saving and emission reduction have received tremendous attentions in the past decade. Use of Variable Speed Drive (VSD) for achieving high system efficiency is an important focusing area. Previously, Permanent Magnet (PM) machine drive system received the most interest as it fits this demand satisfactorily. However, the core material of high performance PM machines – rare earth PM material, experienced a significant increase in price and the price continued to oscillate. Therefore, high performance permanent-magnet-free electrical drive systems become very interesting and start to receive huge investments in recent years.

The Synchronous Reluctance Machine (SynRM) drive system is believed to be a promising candidate. The SynRM has higher torque density and efficiency than that offered by traditional induction motor (IM) [1], [2], while the cost is in the similar range. The difficulty in obtaining a robust variable-speed SynRM drive system is on the control side. Its machine parameters, which are used to derive the necessary information required by the control algorithm, change significantly under different operating conditions, while IM and PM machine do not suffer a lot from this problem. Therefore, a simple and robust control method is one of the key issues in implementing a high performance SynRM drive system.

Using small DC-link capacitor is another attracting point in recent drive system developments. Normally, electrolytic capacitors are used in frequency converters, which may occupy more than 30% of the converter volume. In recent years, there is an increasing trend to replace the electrolytic capacitor with film capacitor, which has a longer lifetime and no explosion risk. Furthermore, studies show that the required total capacitance of the dc-link equipped with film capacitors is much smaller than that equipped with electrolytic capacitors [3], [4]. It is then possible to achieve a compact design by using film capacitors, especially when the voltage and power ratings are high [3], [4]. This is known as small dc-link drive and is obtaining increasing attentions in recent years.

All the above considerations motivate the development of a robust, compact drive system equipped with SynRM and small dc-link, which has been investigated in this project.

1.2   Project Objectives

In a variable-speed SynRM drive system, rotor motion information, e.g. rotor position and speed, is essential to ensure the synchronization between the rotor motion and the rotating stator magnetic field. The motion information may be obtained by auxiliary devices (e.g. resolver, or encoder), but due to some well-known reasons [5] (e.g. low installation cost, electromagnetic interference prevention, etc.), it is much preferred to drive the machine system in an encoderless (sensorless) manner.

Besides the sensorless control of the drive system, existing investigations also show stabilization problems of small dc-link drive system, due to the resonance between the grid side inductance and the DC-link capacitor [18]-[32]. Active damping methods should be considered to damp the resonance and to achieve a good balance between the machine- and grid-sides performances.

Therefore, the whole project can be broken into the following objectives:
- Performance analysis of sensorless operation of SynRM drive with normal DC-link inverter;
- General analysis of the system stability of small DC-link drives;
- Small DC-link drive with active damping techniques.

2 IMPLEMENTATION

All the investigations presented in this project are examined and verified experimentally.

2.1 Overview of the Test Platform

The system setup is shown in Fig. 2.1 and Fig. 2.2. A three-phase frequency converter connected to the grid is used to drive the SynRM, which is loaded by the load system. The gate signals to the inverter are provided by the controller. Machine currents and converter dc-link voltage are acquired by the controller through current and voltage sensors. An encoder is connected to the non-drive-end of SynRM to provide reference rotor position information. A PC is connected to exchange data and control signals with the controller.
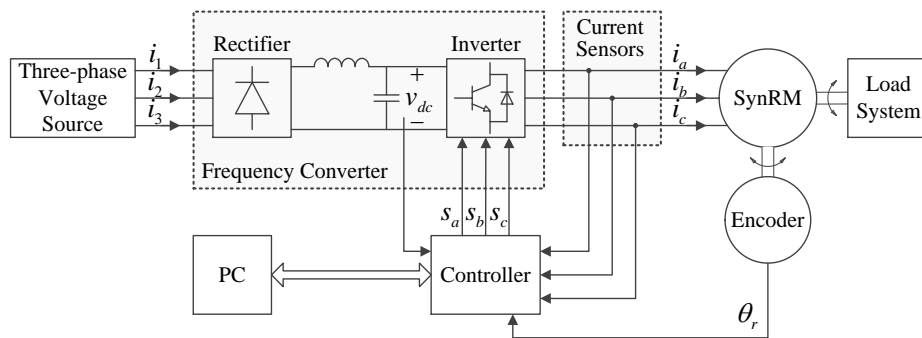

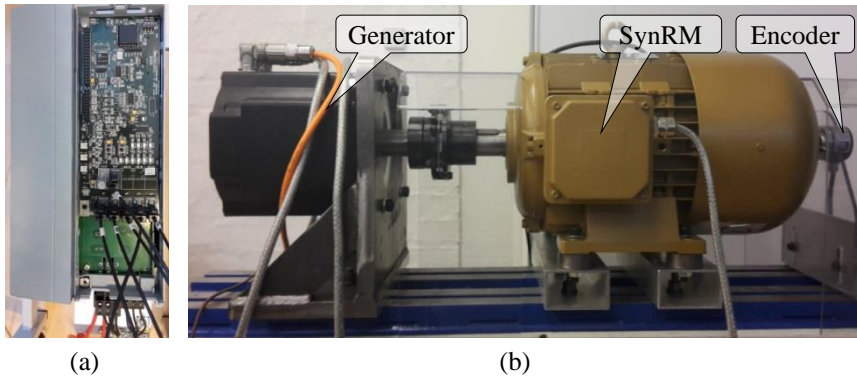Fig. 2.1. Block diagram of the SynRM drive system setup.

(a)   (b)

Fig. 2.2. Pictures of the system setup. (a) Frequency converter. (b) Machine test bench.

2.2 Drive System

2.2.1 Frequency Converter

The 7.5kW (400V) frequency converter accepts input of "3×380-500V, 50/60Hz 14.4/13.0A", and the output is "3×0-Vin 0-590Hz 16/14.5A", where "Vin" means the input voltage of the frequency converter. The type code of the frequency converter used in this project is FC-302P7K5T5E20H1BGXXXXSXXXXAXBXCXXXXDX, and the power module used in the frequency converter is DP50H1200T101729.

The control panel of the commercial frequency converter is replaced with an interface and protection card (IPC) as shown in Fig. 2.2 (a), which can receive the control/gate signals from the control-

ler. The inverter dead time can be set by the IPC with the options of 2μs, 2.5μs, 3μs or 4μs. In this project, 2μs dead time is used.

2.2.2 Synchronous Reluctance Machine

The parameters of the 5.5kW SynRM at rated condition are listed in Table 2.1. Studies have shown that the machine inductances vary for different load conditions due to the self- and cross-saturation effects [6]-[7], the d- and q-axes inductances at different load conditions are tested and shown in Fig. 2.3.

Table 2.1. Parameters of SynRM

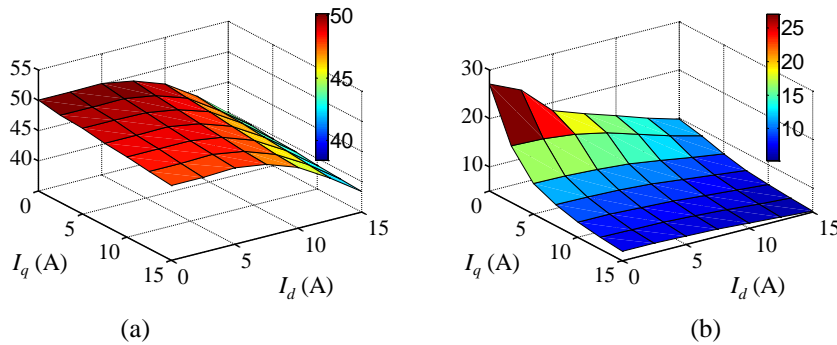| Rated power	5.5 kW	Rated frequency	50 Hz
Rated voltage	353 V	Power factor	0.69
Rated current	13.9 A	Stator resistance	0.38 Ω
Rated speed	1500 rpm	Inertia	1.9×10^{-2} kg·m^2
Rated torque	35.0 N·m	Pole pairs	2

Fig. 2.3. Machine inductance at different load conditions. (a) d-axis inductance. (b) q-axis inductance.

2.2.3 Sensor Box

The sensor box contains three current transducers (LA 55-P) and one voltage transducers (LV 25-P).

The measuring resistance of LA 55-P is designed to be about 21.2Ω, so that the output voltage is in the range of ±1.5V. The number of windings is set to be two, which corresponds to a current measuring range of ±25A peak.

The measuring resistance of LV 25-P at primary side is designed to be 80kΩ, so that it can measure up to 800V within primary nominal current limit (10mA). The measuring resistance at the secondary side is 60Ω to give a ±1.5V voltage output.

2.2.4 Controller

The whole controller includes a digital signal processor (DSP), a USB docking station, and an interface board as shown in Fig. 2.4. The interface board contains the connection ports with other devices, including encoder, frequency converter, and sensor box. Since the voltage signals from sensors are at the level of ±1.5V, level shifting circuits are integrated in the interface board to shift the input voltage to 0-3V, which is required for ADC inputs of DSP.
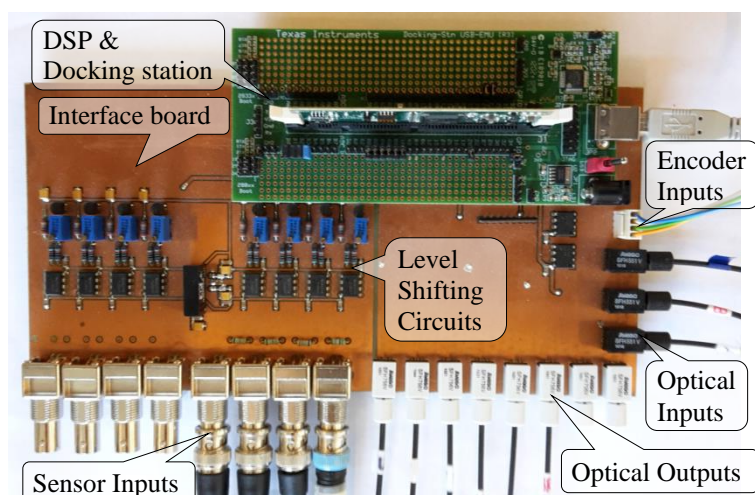
Fig. 2.4. Controller of the drive system.

2.3 Load System

The load system contains a generator, a three-phase transformer, and a three-phase resistor bank. A PM machine is used to serve as the generator. The generated three-phase voltage is increased by the transformer to ensure that the resistor bank can consume enough power even at low speed operation range. The parameters of the PM machine are listed in Table 2.2.

Table 2.2. Parameters of PM Generator

Rated power	6.67 kW	Standstill torque	29.4 N·m
Rated torque	18.2 N·m	Standstill current	18.7 A
Rated speed	3500 rpm	Stator resistance	0.35 Ω
Rated voltage	480 V	Inertia	6.5×10^{-3} kg·m^2
Torque constant	1.58	Pole pairs	5

According to the manual of the PM machine, the standstill torque and current can be maintained indefinitely at a speed between 0 and 100rpm and rated ambient conditions. However, since it is only for lab experiments rather than continuous operation, the standstill torque can be achieved even for speed up to 1500rpm during the test. Therefore, the SynRM can be loaded to about 29.4Nm by the load system, which corresponds to about 12A load current of SynRM.

2.4 Small DC-Link Drive

To carry out the studies for small dc-link drive, a 7.5kW Danfoss VLT® AutomationDrive FC 302 frequency converter is modified. The original electrolytic capacitors (two 450V 1000μF connected in series) in the dc-link are replaced with a film capacitor (1200V 14μF), while the dc-chokes in the dc-link are removed. A three-phase line reactor (3×1.47mH) is connected between the grid and the frequency converter to perform the function of dc-chokes as well as the soft grid. The system circuit diagram of the small dc-link drive is illustrated in Fig. 2.5, where R_g and L_g are grid resistance and inductance, respectively.

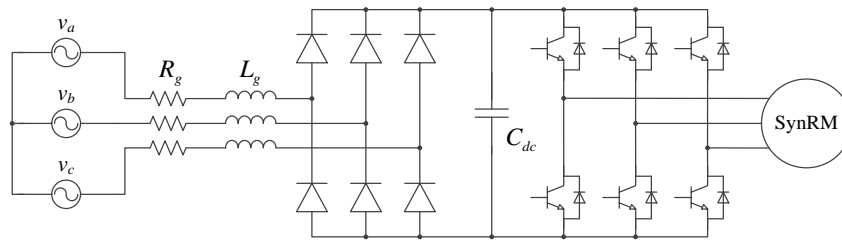Fig. 2.5. System circuit diagram of the small dc-link drive.

Fig. 2.6 shows the modification to the frequency converter. It can be seen that the dc-chokes in Fig. 2.6 (a) have been removed and the space is occupied by the film capacitor shown in Fig. 2.6 (b).
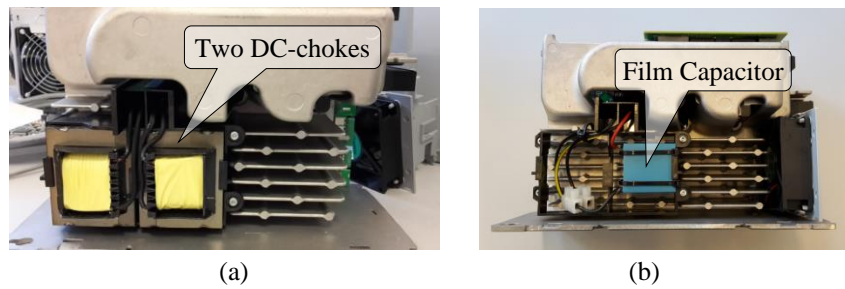

(a)

(b)

Fig. 2.6. Modification of the frequency converter. (a) Original converter with dc-chokes in the dc-link. (b) Modified converter with film capacitor.

3 POSITION-SENSORLESS CONTROL

The position-sensorless control of the SynRM drive system equipped with normal DC-link converter is investigated first. The field-oriented control (FOC) together with the space vector modulation (SVM) technology is implemented [8]. Position sensorless control technique based on the machine fundamental voltage such as electromotive force (EMF) or flux linkage is adopted.

3.1 Control Scheme

The block diagram of the control scheme is illustrated in Fig. 3.1. The three switches (S1, S2, and S3) are connected to terminal 1 during the startup procedure and are switched to terminal 2 during normal FOC operation. An open-loop *I-f* startup strategy is used to accelerate the SynRM from standstill to a specific predetermined speed, e.g. 20% of the machine rated speed, and then switched to the closed-loop FOC operation. This *I-f* method was initially introduced for PMSM and detailed stability analysis and design guidelines were given in [9].
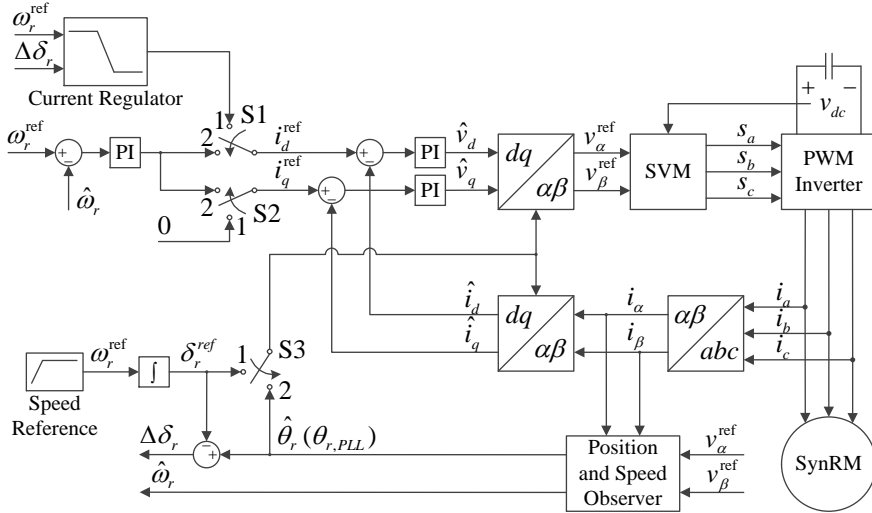

Fig. 3.1. Block diagram of the position-sensorless FOC of SynRM with open-loop *I-f* startup method.

The electromagnetic torque of the SynRM can be expressed as [1], [2]:

$$T_{em} = \frac{3}{2} p \left(L_d \left(i_d, i_q \right) - L_q \left(i_d, i_q \right) \right) i_d i_q, \tag{3.1}$$

where p is the machine number of pole-pairs, i_d and i_q are machine d- and q-axes currents, $L_d (i_d, i_q)$ and $L_q (i_d, i_q)$ are machine d- and q-axes inductances that are current dependent due to the self- and cross-saturation effects [6], [7].

For fixed machine inductances L_d and L_q, in order to achieve maximum torque-per-ampere value as well as high machine energy efficiency, the optimal choices of i_d and i_q are recommended as [1], [2]:

$$i_d = i_q = I_s / \sqrt{2}, \tag{3.2}$$

where I_s is the magnitude of the machine current vector. For real situations with current dependent machine inductances, it is still a convenient choice. Thus, it can be seen in Fig. 3.1 that $i_d^{\text{ref}} = i_q^{\text{ref}}$ during normal FOC operation.

3.2 Position and Speed Observer

The conventional machine voltage model represented in the stationary $\alpha\beta$-reference frame can be expressed as:

$$\bar{v}_{\alpha\beta} = R_s \bar{i}_{\alpha\beta} + \frac{d}{dt}\bar{\lambda}_{\alpha\beta}, \tag{3.3}$$

where R_s is the stator phase resistance, $\bar{v}_{\alpha\beta}$, $\bar{i}_{\alpha\beta}$, and $\bar{\lambda}_{\alpha\beta}$ are the machine stator voltage vector, current vector, and flux linkage vector, respectively. Thus, the machine flux linkage vector in the stationary $\alpha\beta$-reference frame can be calculated as:

$$\bar{\lambda}_{\alpha\beta} = \int \left(\bar{v}_{\alpha\beta} - R_s \bar{i}_{\alpha\beta} \right) dt . \tag{3.4}$$

Instead of the integration of the voltage/EMF information in (3.4), the flux linkage can be obtained alternatively from the machine currents and inductances information, which is known as the machine current model:

$$\bar{\lambda}_{\alpha\beta} = \bar{\lambda}_{dq} e^{j\theta_r} = \left(\lambda_{pm} + L_d i_d + j L_q i_q \right) e^{j\theta_r}, \tag{3.5}$$

where λ_{pm} is the magnitude of the possible rotor PM flux-linkage, and θ_r is the machine rotor position that is aligned with machine d-axis.

It can be obtained from (3.5) that the rotor position θ_r can be calculated as:

$$\theta_r = \arg\left(\bar{\lambda}_{\alpha\beta} - L_q \bar{i}_{\alpha\beta} \right) = \tan^{-1} \frac{\lambda_\beta - L_q i_\beta}{\lambda_\alpha - L_q i_\alpha} . \tag{3.6}$$

Based on (3.4) to (3.6), the machine position and speed observer can be built as illustrated in Fig. 3.2, which includes a closed-loop flux observer and the open-loop position and speed estimator.
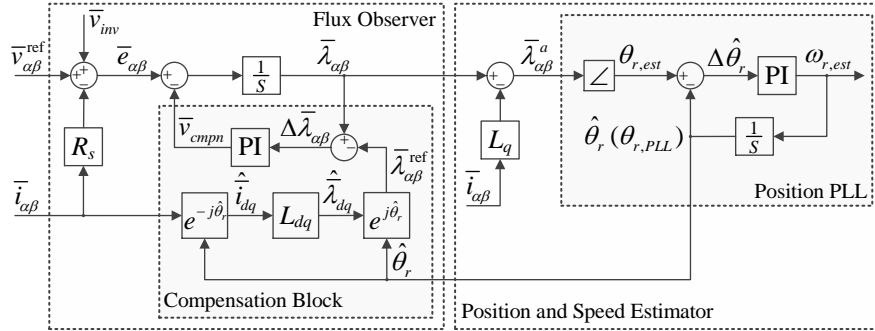

Fig. 3.2. Block diagram of the position and speed observer.

It can be seen that the machine current model serves as the reference model and the machine voltage model serves as the adjustable model in the MRAS flux observer. A PI regulator based adaptation mechanism is chosen, through which the adjustable voltage model is dominant at middle-high speed operation range and the current model is dominant at low speed range [10], [11]. The output compensation signal $\bar{v}_{cmpn}$ is the feedback to the adjustable voltage model to compensate various errors caused by integration dc-offset, stator resistance variation, etc. The voltage error caused by inverter nonlinearity $\bar{v}_{inv}$ ([14]-[16]) is compensated in the machine voltage model as shown in Fig. 3.2. Moreover, since the machine inductances can vary significantly due to the self- and cross-saturations as shown in Fig. 2.3, a lookup table is usually used to obtain more accurate machine inductances used in the machine current model [12], [13].

3.3 System Oscillation Phenomena

The control scheme illustrated in Fig. 3.2 is realized in DSP and verified experimentally with the control parameters listed in Table 3.1. A new system oscillation phenomenon is observed. Fig. 3.3 (a) shows the experimental performance at 600rpm 10A load condition. A clear dc-offset in the estimated machine flux linkage (λ_α and λ_β) and oscillations in the estimated ($\hat{n}_r$) and real (n_r) machine speeds can be observed in Fig. 3.3. The sound level of the acoustic noise is significantly increased during the experiments, which means this system oscillation is unacceptable. In fact, it can be observed that the system is oscillating in a small range at 300rpm noload condition as shown in Fig. 3.3 (b). This phenomenon has rarely been reported before. It means that the closed-loop flux observer illustrated in Fig. 3.2, which has been widely used in [10]-[12], cannot always work properly. Dc-offset can appear in the estimated flux linkage under certain conditions, which cannot be eliminated any longer by the flux observer itself. The dc-offset in the flux linkage will finally result in the system oscillation, which can be very harmful to the machine drive system. Therefore, solutions to eliminate the oscillation are needed.

Table 3.1. Control Parameters

Switching frequency	10 kHz	Speed regulator PI	$k_{pw} = 0.5$, $k_{iw} = 1.0$
Flux observer PI	$k_{p\lambda} = 50$, $k_{i\lambda} = 100$	Current regulator PI d-axis	$k_{pd} = 15$, $k_{id} = 1500$
Position PLL PI	$k_{pp} = 1000$, $k_{ip} = 50000$	Current regulator PI q-axis	$k_{pq} = 15$, $k_{iq} = 1500$
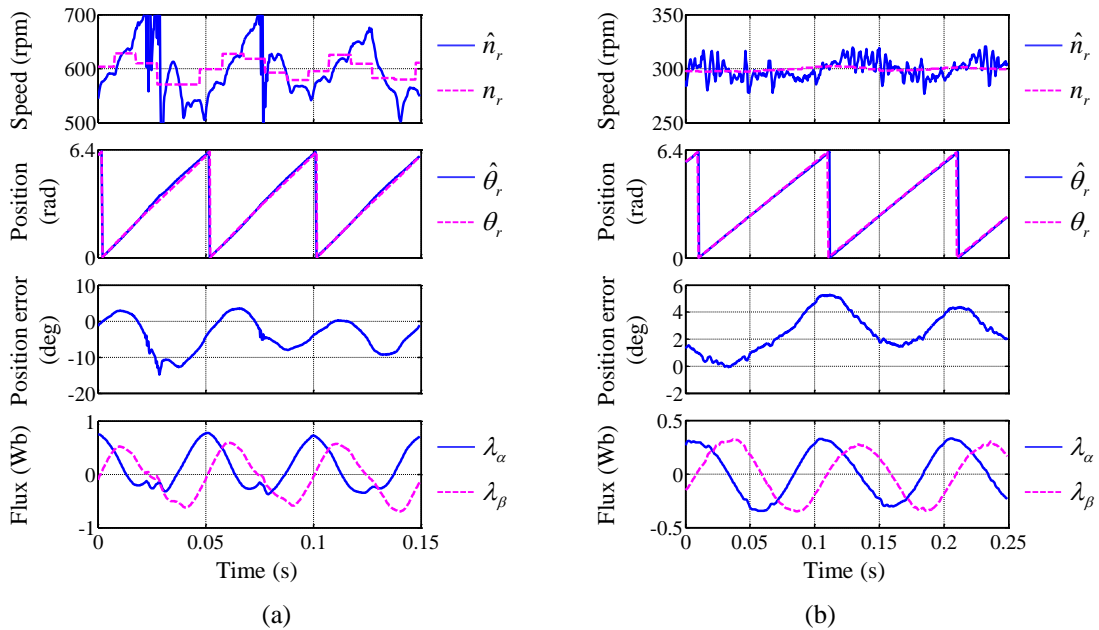
Fig. 3.3. Sensorless FOC experimental performance when system oscillating. (a) 600rpm 10A load. (b) 300rpm noload.

3.4 Proposed Solutions

3.4.1 Solution with PR Controller

To solve the problem of the system oscillating, it is straightforward to consider removing the dc-offsets in the flux linkage by a dc-offset remover (DCR), e.g. HPF or band pass filters (BPF). Since the adjustable voltage model is dominant in most of the operation range, the DCR is added in the

compensation block of the flux observer to remove the dc-offset in $\bar{\lambda}_{\alpha\beta}^{\text{ref}}$ as illustrated in Fig. 3.4. In this way, the necessary harmonic information can be kept in the final estimated flux linkage $\bar{\lambda}_{\alpha\beta}$ to ensure the machine dynamic performance.
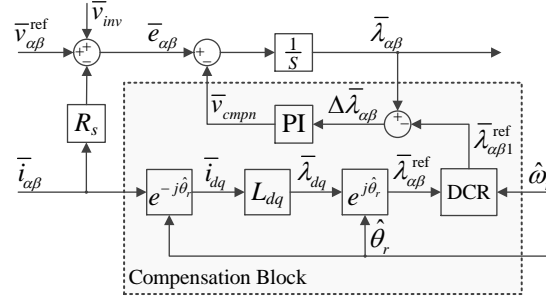

Fig. 3.4. Modified closed-loop flux observer with dc-offset remover (DCR).

However, it is found that removing only the dc-offsets by using HPFs may not be sufficient enough to stabilize the system. This might be because of there are also significant second order harmonics in the flux linkage when system is oscillating. Therefore, an effective way could be to extract only the fundamental components of $\bar{\lambda}_{\alpha\beta}^{\text{ref}}$ by using BPFs. Then the reference flux linkage after the dc-offset remover ($\bar{\lambda}_{\alpha\beta1}^{\text{ref}}$) will be pure sinusoidal signals. It should be point out that even the higher order components of $\bar{\lambda}_{\alpha\beta}^{\text{ref}}$ is eliminated by using BPFs for dc-offsets removal, the influence to the final output of the modified closed-loop flux observer is very limited. This is because that the PI regulator and the integrator in the closed-loop flux observer form a PLL structure, which can perform like a LPF. Thus the high order harmonics of the difference between $\bar{\lambda}_{\alpha\beta}$ and $\bar{\lambda}_{\alpha\beta1}^{\text{ref}}$ will be greatly damped, especially when the cutoff frequency of the PLL is low. The high order harmonics in the compensation signal $\bar{v}_{cmpn}$ give very little influence on the high order harmonics in the signal $\bar{e}_{\alpha\beta}$. Thus, little information is lost and the machine dynamic performance can be maintained. This is why the BPFs are introduced in the compensation block rather than other options.

A non-ideal proportional-resonant (PR) controller can be a good candidate to serve as the BPF to obtain the required fundamental component [17]. Fig. 3.5 shows the sensorless FOC experimental performance with non-ideal PR controller for dc-offset removal. It can be seen that the flux linkage is close to pure sinusoidal, and speed ripples are limited to a very narrow band.

Table 3.2 shows the estimated position error $\Delta\theta_r$ at different operation conditions at steady state with non-ideal PR controller for dc-offset removal. The estimated position error $\Delta\theta_r$ is represented in the form of $med \pm amp$ as indicated in Fig. 3.5 (a), where med means the median value of the maximum and minimum positive errors and amp is the amplitude of the variation part. It can be seen that the position errors have a very narrow variation band, which means that the dc-offsets in the estimated flux linkage and system oscillation phenomenon is removed.

Table 3.2. Position Errors at Different Operation Conditions

Operation Conditions	Position Error $\Delta\theta_r$ [°]	
	PR controller	Adaptive PI
20% n_{rt} with noload	1.37 [a] ± 0.52 [b]	1.28 ± 0.72
40% n_{rt} with noload	4.37 ± 0.50	2.40 ± 1.87
80% n_{rt} with noload	1.99 ± 0.41	-0.12 ± 0.60
20% n_{rt} with 10A load	-1.15 ± 0.30	-0.22 ± 0.43
40% n_{rt} with 10A load	0.53 ± 0.44	-0.10 ± 0.40
80% n_{rt} with 10A load	-1.80 ± 0.50	-1.84 ± 0.56

[a] Median value (*med*) of the maximum and minimum position error
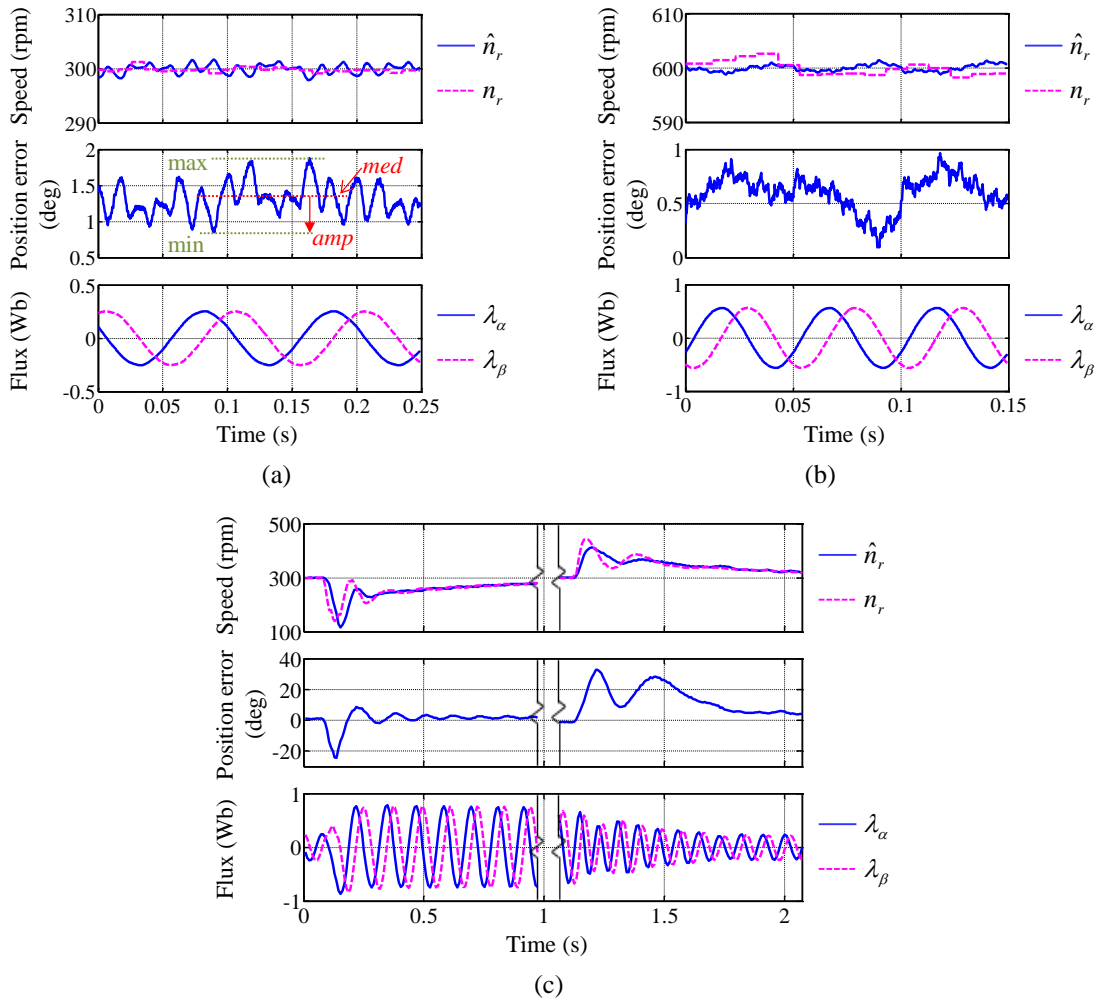[b] Half of the difference between the maximum and minimum position error (*amp*)

Fig. 3.5. Sensorless FOC experimental performance with non-ideal PR controller. (a) 300rpm noload. (b) 600rpm 10A load. (c) 12A step load on and off at 300rpm.

3.4.2 Solution with Adaptive PI Controllers

Another possible way to solve the system oscillation is to increase the damping factor of the oscillations. It is found that reducing the oscillating components in $\hat{\lambda}_d$ and $\hat{\lambda}_q$, which are caused by the oscillating $\hat{i}_d$ and $\hat{i}_q$, could help to reduce the distortion of $\bar{\lambda}_{\alpha\beta}^{\text{ref}}$. Since $\hat{i}_d$ and $\hat{i}_q$ are equal to each other, and L_d is much larger than L_q, $\hat{\lambda}_d$ is dominant in the flux linkage vector. Reducing the oscillation in $\hat{i}_d$ could be considered as a solution. This can be achieved by reducing the PI parameters of the speed regulator and the d-axis current regulator. The reduced dc-offset in the reference machine current model will be reflected to the machine voltage model through the compensation block. Besides, further decay and phase delay of the oscillating components may be introduced by the position PLL. The decayed position and speed oscillations will be fed back and the system may finally settle in a steady-state condition where the oscillations are greatly suppressed.

The above idea is implemented in the real system by using the adaptive PI controllers (including the speed and d-axis current controllers), where the PI parameters are adjusted according to the deviation between the estimated speed feedback $\hat{\omega}_r$ and the reference speed ω_r^{ref}. Small PI parameters (e.g. k_{pw}=0.3, k_{iw}=0.6, k_{pd}=10, and k_{id}=100) are used when the difference between $\hat{\omega}_r$ and ω_r^{ref} are

small, e.g. below 5% of ω_r^{ref}. When the difference between $\hat{\omega}_r$ and ω_r^{ref} increases during fast mechanical dynamics (e.g. step load conditions), PI parameters are increased linearly (such as $k_{pw}=0.3+0.3\times|\hat{\omega}_r-\omega_r^{\text{ref}}|$, $k_{pd}=10+5\times|\hat{\omega}_r-\omega_r^{\text{ref}}|$) in order to provide faster response. Moreover, the PI parameters of the q-axis current controller are always set to a high level ($k_{pq}=15$ and $k_{iq}=1500$) in order to achieve satisfactory system dynamic performance. Fig. 3.6 shows the sensorless FOC experimental performance with the inverter voltage drop compensation and adaptive PI controllers at different operating conditions. It can be seen that the system oscillation is nearly eliminated. The position error at different operation conditions with adaptive PI controllers are listed in Table 3.2 as well. It can be seen that the band of the position errors is narrow, especially for high speed and load conditions where the amplitude of $\hat{\lambda}_d$ is high and the influence caused by possible oscillation is negligible.
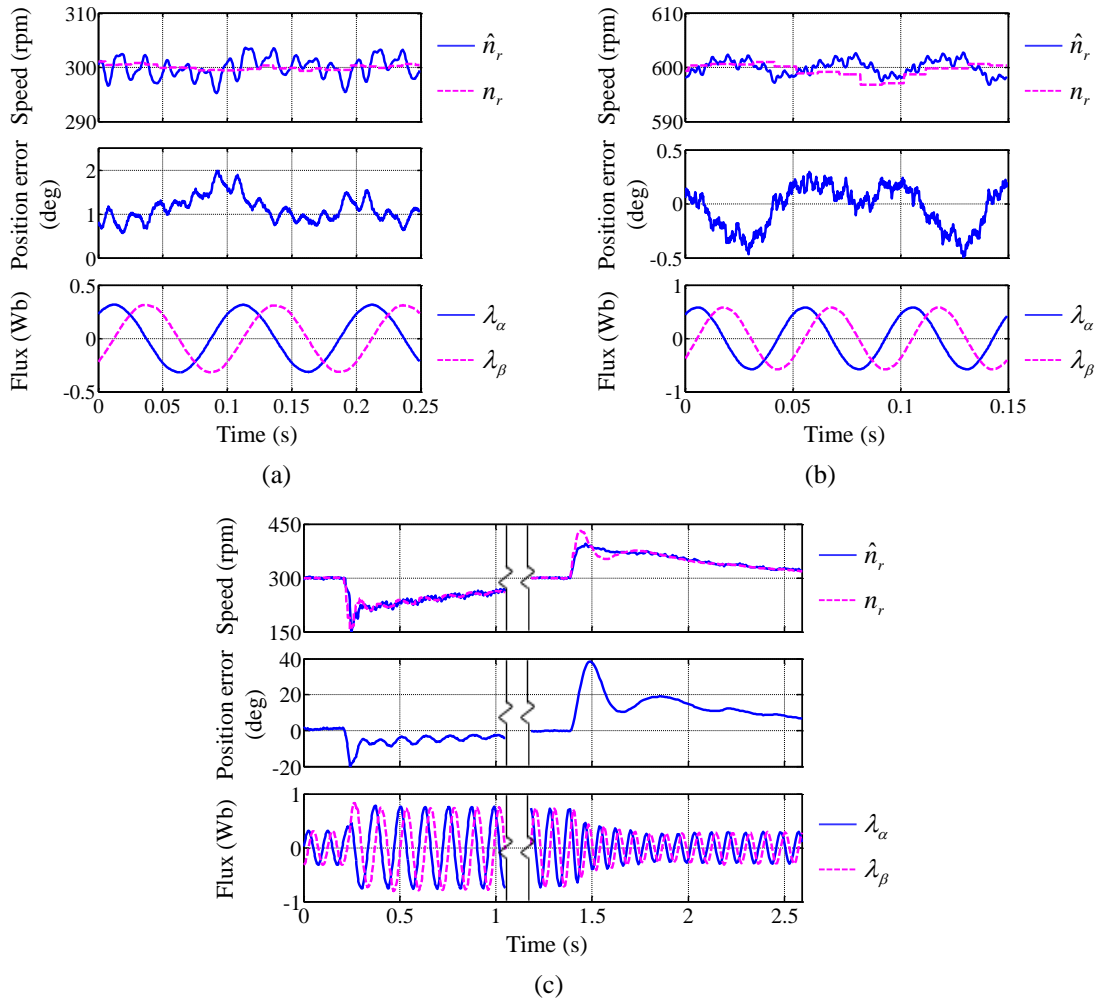

Fig. 3.6. Sensorless FOC experimental performance with adaptive PI controllers. (a) 300rpm noload. (b) 600rpm 10A load. (c) 12A step load on and off at 300rpm.

3.5 Summary

The position estimation algorithm via flux linkage is carried out and has been fully tested. Though the closed-loop flux observer is widely used in various types of machine drives and can provide satisfactory performance, it is found that it cannot always work properly, especially at the condition where the magnitude of the flux linkage vector is low and ambiguous compared to the error- or noise- signals. The compensation block in the closed-loop flux observer may fail in removing the dc-offset, and system oscillation phenomenon may then occur. Solutions to cope with this oscillation phenomenon are proposed to eliminate or suppress this harmful system oscillation. The experimental verifications show that satisfactory performances can be achieved by using the proposed solutions.

4 SMALL DC-LINK SYSTEM ANALYSIS

The characteristics of the small dc-link drive are analyzed, which provides a solid theory funda-tion for further investigations.

4.1 System Analysis

The simplified equivalent circuit of the drive system is illustrated in Fig. 4.1 [18]-[28], where i_{gd} is the input current of the dc-link on the gird side, and i_{inv} is the output current to the inverter. The diode, which represents the uni-directional current flow of the diode rectifier, can be removed for continuous i_{gd}.
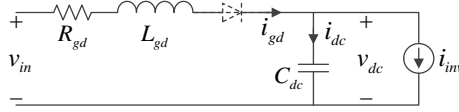

Fig. 4.1. Simplified equivalent circuit model of the drive system.

The second order system described by the simplified equivalent circuit shown in Fig. 4.1 can be expressed as [18], [20]-[23]:

$$L_{gd} \frac{di_{gd}}{dt} = v_{in} - R_{gd} i_{gd} - v_{dc} \tag{4.1}$$

$$C_{dc} \frac{dv_{dc}}{dt} = i_{gd} - i_{inv} . \tag{4.2}$$

The equivalent resistance R_{gd} and inductance L_{gd} can be obtained by

$$R_{gd} = 2R_g + \frac{3\omega_g L_g}{\pi}, \ L_{gd} = 2L_g , \tag{4.3}$$

where ω_g is the grid angular frequency, and $3\omega_g L_g/\pi$ represents the nonohmic voltage drop caused by the diode communication [18], [20], [21].

Theoretically, when the motor draws a constant power P_L from the inverter, which is known as constant power load (CPL), the inverter current i_{inv} linearized at V_{dc} can be expressed as [21]-[23]:

$$i_{inv} = I_{inv} + \tilde{i}_{inv} = \frac{P_L}{v_{dc}} = \frac{P_L}{V_{dc} + \tilde{v}_{dc}} \approx \frac{P_L}{V_{dc}} - \frac{P_L}{V_{dc}^2} \tilde{v}_{dc} = \frac{2P_L}{V_{dc}} - \frac{P_L}{V_{dc}^2} v_{dc} , \tag{4.4}$$

where I_{inv} and $\tilde{i}_{inv}$ are the large and small signals of the inverter current i_{inv}, V_{dc} and $\tilde{v}_{dc}$ are the large and small signals of the dc-link voltage v_{dc}, respectively. The impedance of the inverter with CPL is:

$$Z_{inv} = \frac{\tilde{v}_{dc}}{\tilde{i}_{inv}} = -\frac{V_{dc}^2}{P_L} , \tag{4.5}$$

which is a negative value.

By submitting (4.4) into (4.1) and (4.2), it can be obtained that:

$$\frac{d^2v_{dc}}{dt^2} + \left(\frac{R_{gd}}{L_{gd}} - \frac{P_L}{C_{dc}V_{dc}^2}\right)\frac{dv_{dc}}{dt} + \frac{1}{L_{gd}C_{dc}}\left(1 - \frac{R_{gd}P_L}{V_{dc}^2}\right)v_{dc} = \frac{1}{L_{gd}C_{dc}}v_{in} . \tag{4.6}$$

The following characteristic equation of the second order system in Laplace domain can be obtained [21]-[24]:

$$s^2 + \underbrace{\left(\frac{R_{gd}}{L_{gd}} - \frac{P_L}{C_{dc}V_{dc}^2}\right)}_{a_{10}}s + \underbrace{\frac{1}{L_{gd}C_{dc}}\left(1 - \frac{R_{gd}P_L}{V_{dc}^2}\right)}_{a_{20}} = 0 . \tag{4.7}$$

According to Routh-Hurwitz stability criterion, the system is stable when a_{10} and a_{20} are greater than zero. Normally, $|Z_{inv}|$ is much greater than R_{gd}, i.e. a_{20} is greater than zero. Then, the system stability is depending on a_{10}. The system is stable if $a_{10} > 0$, i.e.

$$\frac{R_{gd}}{L_{gd}} > \frac{P_L}{C_{dc}V_{dc}^2} \iff \frac{C_{dc}}{P_L} > \frac{L_{gd}}{R_{gd}V_{dc}^2} . \tag{4.8}$$

The system is stable when the criterion of (4.8) is satisfied, which is the condition for normal frequency converters with large electrolytic capacitors. However, it may be not true for small dc-link drives. When the criterion of (4.8) is not satisfied, the dc-link voltage and grid currents will become unstable or oscillating [23]-[25]. The overvoltage may destroy the IGBTs and capacitors, and the lifetime of the capacitor will be reduced due to the voltage oscillation.

The angular frequency of the dc-link voltage oscillation can be calculated analytically according to the system characteristic equation (4.7). And it can be approximated by the angular resonant frequency of the LC circuit shown in Fig. 4.1, i.e. $1/(L_{gd}C_{dc})^{1/2}$ [19]-[21].

4.2 System Performance

For a 50Hz 380V supply and a 5.5kW SynRM load, the capacitance needed to operate the system stably during the whole power range is about 126μF according to (4.8). The modified small dc-link drive described in section 2.4 has only 14μF dc-link capacitance, which means that the system may become unstable when the load increases to a certain level.

Fig. 4.2 shows the system performance when the machine operates at 1500rpm and 12A load (machine phase RMS current). The dc-link voltage variation has a peak-to-peak voltage of about 206V. Besides the rectified voltage component (f_{rect}=300Hz), apparent 600Hz ($2f_{rect}$) oscillations can be observed.

Fig. 4.2. Small dc-link drive system experimental results at 1500rpm 12A load without active damping control. (a) Waveforms. (b) Spectrum without dc component.

The total harmonic distortion (THD) and the partially weighted harmonic distortion (PWHD) [29] of the grid current are 69.0% and 67.0%, respectively. The machine current THD is 3.7%.

Fig. 4.3 shows the dc-link voltage and grid current when the machine operates at 900rpm and 7.5A load. The dc-link voltage variation has a peak-to-peak voltage of about 137V. The THD and PWHD of the grid current increase to 112.5% and 129.9%, respectively. The machine current THD is 3.2%.

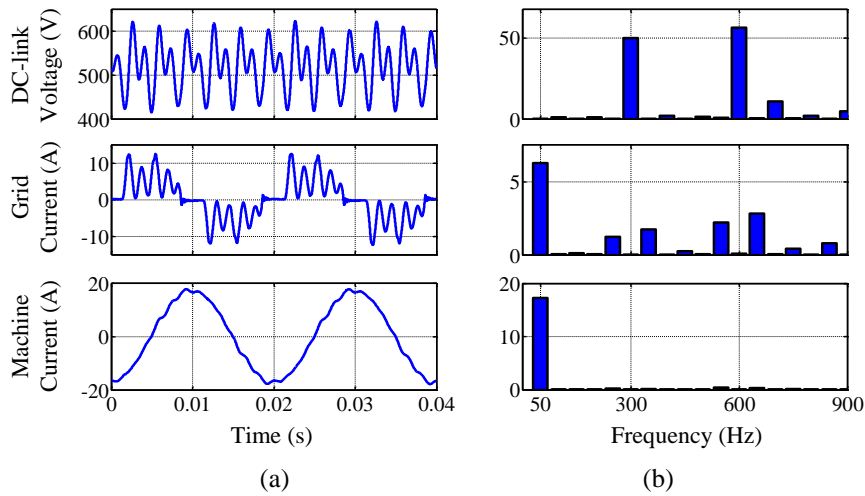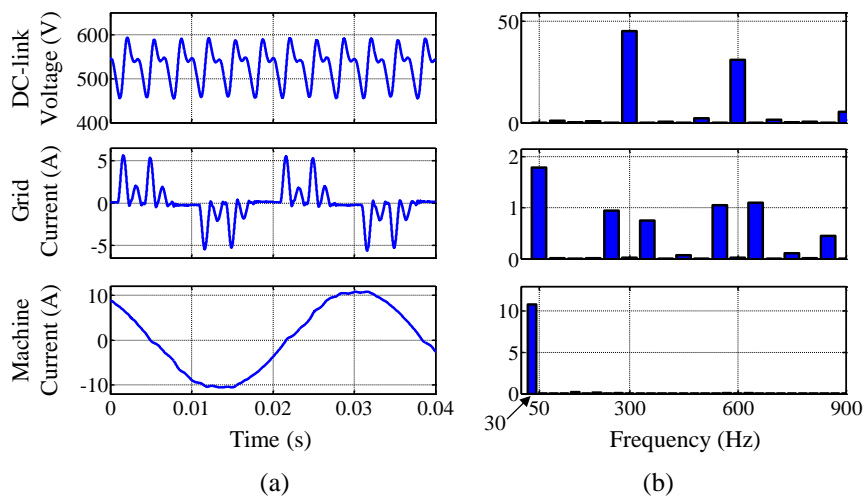Fig. 4.3. Small dc-link drive system experimental results at 900rpm 7.5A load without active damping control. (a) Waveforms. (b) Spectrum without dc component.

It can be observed from Fig. 4.2 and Fig. 4.3 that the dc-link voltage variation increases as the machine load increases, which agrees with (4.8). The grid current THD and PWHD values are high and may not be able to satisfy the IEC requirements.

4.3 Summary

The small dc-link drive system is analyzed. It is shown that the reduced dc-link capacitance of the small dc-link drive may result in dc-link voltage oscillation, which is harmful to the drive system and will reduce the service lifetime. Moreover, the grid current with amplified higher order harmonics around the resonant frequency may fail to meet the requirements from the standards/regulations. Therefore, techniques to stabilize the dc-link voltage are required, so that the system performance can meet the expectations.

5 ACTIVE DAMPING METHODS

It has been shown in (4.5) that the inverter has a "negative impedance" characteristic under CPL condition, and its absolute value increases as the load increases. The whole system will become unstable when the load increases to a certain level and the damping factor of the system characteristic equation (4.7) reduces to a negative value. The basic idea of active damping methods is to achieve positive dynamic damping factor by controlling the actual power drawn by the machine from the dc-link [18]-[28]. As the machine input power is no longer constant, machine torque ripple will appear and it is only suitable for applications with moderate machine shaft dynamic requirements. However, as no extra damping circuit is required, it is a cheap solution and is adopted in this project.

5.1 Active Damping Methods

5.1.1 Current Injection Active Damping Control

It is straight forward to control the power drawn by the machine by controlling the torque producing current component directly. Different methods to obtain the proper current reference were proposed [21], [24]-[27]. Taking the method in [21] as an example, a term proportional to the dc-link voltage variation term $\tilde{v}_{dc}$, i.e. the small signal of dc-link voltage, is added/injected to the torque producing current reference i_q^{ref}, which can be expressed as:

$$i_q^{ref} = I_q^{ref} + \tilde{i}_q^{ref} = I_q^{ref} + g_{iq}\tilde{v}_{dc} . \tag{5.1}$$

where I_q^{ref} is the unmodified component, i.e. large signal of i_q^{ref} for steady state operating conditions, and g_{iq} is the gain factor of q-axis injected current term. Similarly, a gain factor g_{id} can be introduced to control the current term injected to d-axis.

Then, i_{inv} linearized at V_{dc} can be calculated as:

$$i_{inv} \approx \frac{P_L}{V_{dc}} + (\frac{3}{2}\frac{V_q g_{iq}}{V_{dc}} - \frac{P_L}{V_{dc}^2})\tilde{v}_{dc} = \frac{P_L}{V_{dc}} + (g - \frac{P_L}{V_{dc}^2})\tilde{v}_{dc} , \tag{5.2}$$

when $\tilde{v}_{dc}/V_{dc}$ approaches zero.

By submitting (5.2) into (4.1) and (4.2), the following characteristic equation of the second order system in the Laplace variable s can be obtained:

$$s^2 + \underbrace{\left(\frac{R_{gd}}{L_{gd}} + \frac{1}{C_{dc}}(g - \frac{P_L}{V_{dc}^2})\right)}_{a_{11}}s + \underbrace{\frac{1}{L_{gd}C_{dc}}\left(1 + R_{gd}(g - \frac{P_L}{V_{dc}^2})\right)}_{a_{21}} = 0 . \tag{5.3}$$

Compared with the original system characteristic equation (4.7), a new term g is introduced in (5.3) when injecting a variation term $\tilde{i}_q^{\text{ref}}$. It can be easily found that when

$$g \geq P_L/V_{dc}^2 , \tag{5.4}$$

a_{11} and a_{21} will be greater than zero and the system is stable according to Routh-Hurwitz stability criterion. Similar criterion can be obtained by repeating the above analysis when injecting in d-axis current reference.

5.1.2 Voltage Injection Active Damping Control

In a real digital control system, it is not easy to achieve ideal current injection due to the bandwidth limitation. Thus, instead of controlling the current reference, active damping methods based on the reference voltage control are suggested [18]-[20], [22], [23], [28].

Similarly as the above current injection method, voltage variation terms $\tilde{v}_d$ and $\tilde{v}_q$ are injected into the machine dq-axes stator voltages to achieve positive dynamic damping factor. The voltage variations terms are defined as [18]:

$$\tilde{v}_d = g_{vd}\tilde{v}_{dc} \text{ and } \tilde{v}_q = g_{vq}\tilde{v}_{dc}, \tag{5.5}$$

where g_{vd} and g_{vq} are the gain factors of d- and q-axes injected voltage terms, respectively.

When $\tilde{v}_{dc}/V_{dc}$ approaches zero, i_{inv} can be calculated as:

$$i_{inv} \approx \frac{P_L}{V_{dc}} + (\frac{3}{2}\frac{I_d g_{vd} + I_q g_{vq}}{V_{dc}} - \frac{P_L}{V_{dc}^2})\tilde{v}_{dc} = \frac{P_L}{V_{dc}} + (g - \frac{P_L}{V_{dc}^2})\tilde{v}_{dc} \ . \tag{5.6}$$

It can be observed that (5.6) has the same form as (5.2). The system characteristic equation identical to (5.3) will be obtained. The same stability criterion (5.4) would be achieved as well.

5.1.3 Virtual Positive Impedance Active Damping Method

The system analysis showed that the "negative impedance" characteristic of the inverter at CPL condition is the root cause of the system instability. Therefore, the system can be stabilized if the "negative impedance" characteristic can be manipulated to perform like positive impedance. The "virtual positive impedance" active damping method is based on such an idea [22].

When the reference dc-link voltage v_{dc}^{ref} that is used to calculate the three-phase duty cycles in the PWM technique is reconstructed from the real dc-link voltage v_{dc} ($v_{dc}=V_{dc}+\tilde{v}_{dc}$) to $V_{dc}-\tilde{v}_{dc}$ as illustrated in Fig. 5.1, the output machine voltage vector becomes $\bar{v}_{abc1}$ instead of the commanded voltage vector $\bar{v}_{abc}$. It can be calculated that:

$$\bar{v}_{abc1} = \frac{\bar{v}_{abc}^{\text{ref}}}{v_{dc}^{\text{ref}}}v_{dc} = \bar{v}_{abc}^{\text{ref}}\frac{V_{dc}+\tilde{v}_{dc}}{V_{dc}-\tilde{v}_{dc}} \ . \tag{5.7}$$
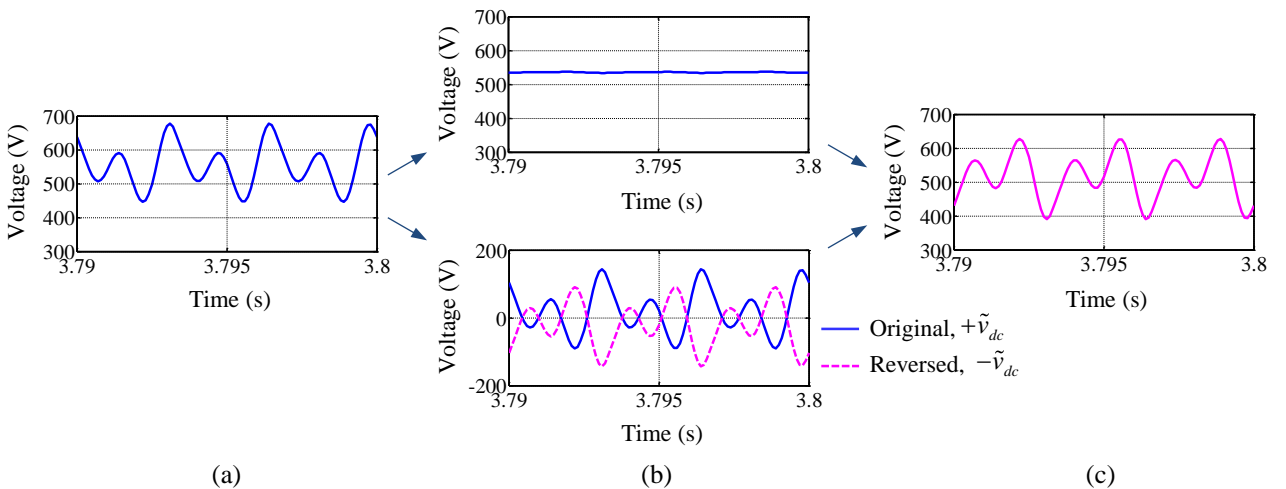

Fig. 5.1. Decomposition and reconstruction of reference dc-link voltage signal v_{dc}^{ref}. (a) dc-link voltage v_{dc}. (b) from top to bottom: dc part (V_{dc}), $\tilde{v}_{dc}$ and reversed $\tilde{v}_{dc}$. (c) reconstructed v_{dc}^{ref} with V_{dc} and reversed $\tilde{v}_{dc}$.

The inverter input current i_{inv} can then be calculated and linearized as:

$$i_{inv} = I_{inv} + \tilde{i}_{inv} = P_L \frac{V_{dc} + \tilde{v}_{dc}}{V_{dc} - \tilde{v}_{dc}} \frac{1}{V_{dc} + \tilde{v}_{dc}} = \frac{P_L}{V_{dc} - \tilde{v}_{dc}} \approx \frac{P_L}{V_{dc}} + \frac{P_L}{V_{dc}^2} \tilde{v}_{dc} = \frac{P_L}{V_{dc}^2} v_{dc}. \tag{5.8}$$

Compared with (4.4), it can be seen that the only difference of (5.8) is that the sign of $\tilde{v}_{dc}$ or v_{dc} is changed, i.e. the impedance now becomes positive. The system characteristic equation can then be expressed as:

$$s^2 + \underbrace{\left(\frac{R_{gd}}{L_{gd}} + \frac{P_L}{C_{dc}V_{dc}^2} \right)}_{a_{12}} s + \underbrace{\frac{1}{L_{gd}C_{dc}} \left(1 + \frac{R_{gd}P_L}{V_{dc}^2} \right)}_{a_{22}} = 0. \tag{5.9}$$

It can be seen that the coefficients a_{12} and a_{22} in (5.9) are always greater than zero and the system is always stable now. Therefore, instead of finding the gain of variation terms, which are system parameters and operating condition dependent, the system can be stabilized by simply reconstructing v_{dc}^{ref} with reversed $\tilde{v}_{dc}$, and a "virtual positive impedance" characteristic can be obtained. Detailed analysis shows that the influence of the "virtual positive impedance" active damping method to the machine variables is equivalent to the q-axis injection.

Furthermore, a factor g_v is introduced to control the deviation between reconstructed v_{dc}^{ref} and v_{dc}, i.e $v_{dc}^{ref} = V_{dc} - g_v \tilde{v}_{dc}$, (5.9) now become:

$$s^2 + \underbrace{\left(\frac{R_{gd}}{L_{gd}} + \frac{g_v P_L}{C_{dc}V_{dc}^2} \right)}_{a_{13}} s + \underbrace{\frac{1}{L_{gd}C_{dc}} \left(1 + \frac{g_v R_{gd}P_L}{V_{dc}^2} \right)}_{a_{23}} = 0. \tag{5.10}$$

The coefficients a_{13} and a_{23} in (5.10) are always greater than zero when $g_v \geq 0$. It can be observed that a stable system can already be achieved when $g_v = 0$, i.e. using V_{dc} to serve as v_{dc}^{ref} is sufficient enough to stabilize the system. However, the damping factor of (5.10) can be increased by increasing g_v, so that the variation terms such as $\tilde{v}_{dc}$ can be suppressed further. But the machine torque ripple will be increased as more oscillating energy is injected into the machine side.

In order to make a clear relation between the meaning and value of the gain factor, a new gain factor g_{v0} is introduced, which is defined as:

$$g_{v0} = g_v + 1. \tag{5.11}$$

Then, $g_{v0} = 0$ means no active damping is applied, since $g_v = -1$ and $v_{dc}^{ref} = v_{dc}$. When $g_{v0} \neq 0$, the deviation between reconstructed v_{dc}^{ref} and v_{dc} is $g_{v0}\tilde{v}_{dc}$. The reverse operation illustrated in Fig. 5.1 corresponds to $g_{v0} = 2$.

5.2 Verifications

5.2.1 Obtaining DC-Link Voltage Variation

Since the dc-link voltage variation term $\tilde{v}_{dc}$ is needed in all the active damping control methods mentioned above, it is a key task to find $\tilde{v}_{dc}$ in the implementation of active damping control. It can be seen in Fig. 5.2 that the dc-link voltage contains three parts: the dc part V_{dc}, the ripple voltage $\tilde{v}_{rip}$

at rectified voltage frequency f_{rect}, and the oscillating term $\tilde{v}_{osci}$ with frequency f_{osci}. It should be noted that $\tilde{v}_{rip}$ is approaching to the rectified voltage variation term $\tilde{v}_{rect}$ as the load increases when the C_{dc} is small.
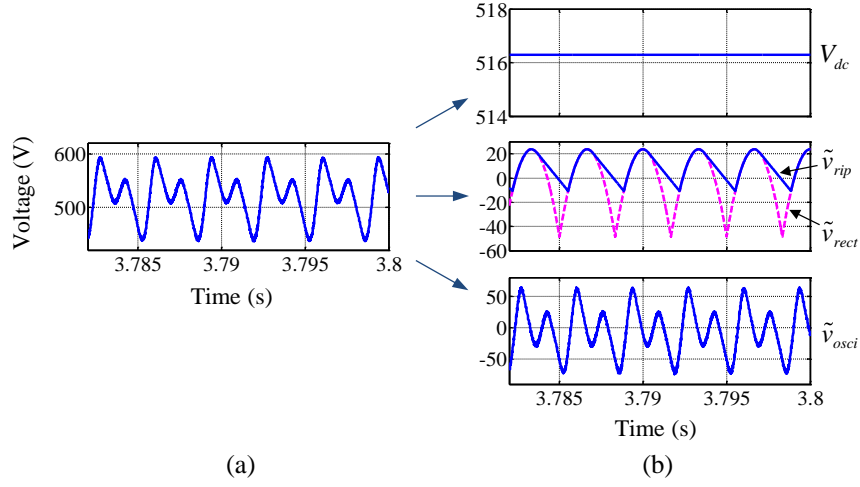

Fig. 5.2. Composition of the dc-link voltage. (a) dc-link voltage v_{dc}. (b)Top: dc part V_{dc}; middle: dc-link ripple voltage $\tilde{v}_{rip}$ and rectified component $\tilde{v}_{rect}$; bottom: dc-link voltage oscillating term $\tilde{v}_{osci}$.

There are briefly two ways to define the dc-link voltage variation term $\tilde{v}_{dc}$. One way is:

$$\tilde{v}_{dc} = v_{dc} - V_{dc} = \tilde{v}_{rip} + \tilde{v}_{osci}. \tag{5.12}$$

It is the simplest way as V_{dc} can simply be obtained by using a LPF. However, since $\tilde{v}_{rip}$ is included in $\tilde{v}_{dc}$, the active damping method will try to damp it as well. For machine drive system, this will result in large machine current ripple at rectified voltage frequency f_{rect}. Large torque ripple at the same frequency will be generated, which may reduce the bearing lifetime and increase the machine noise level. Therefore, instead of damping both $\tilde{v}_{rip}$ and $\tilde{v}_{osci}$, it is a better choice to damp $\tilde{v}_{osci}$ only, i.e. $\tilde{v}_{dc}$ can be defined as:

$$\tilde{v}_{dc} = \tilde{v}_{osci} = v_{dc} - V_{dc} - \tilde{v}_{rip}. \tag{5.13}$$

It is not an easy task to find $\tilde{v}_{rip}$ from v_{dc}. However, due to the fact that the dc-link ripple voltage $\tilde{v}_{rip}$ is close to the rectified component $\tilde{v}_{rect}$ at heavy load conditions for small dc-link drive, $\tilde{v}_{rect}$ can be used to simulate $\tilde{v}_{rip}$. A complicate method based on PLL and FLL trackers is introduced in [33], which can calculate V_{rect} ($V_{dc}+\tilde{v}_{rect}$) from v_{dc} by identifying the amplitude, frequency, and phase angle of V_{rect}. But the error increases as the load decreases. An alternative method is to use the fundamental component of $\tilde{v}_{rip}$, which is a pure sinusoidal signal at frequency f_{rect}, to approximate $\tilde{v}_{rip}$ [22]. This fundamental component $\tilde{v}_{rip1}$ can be simply obtained by using a BPF, such as a PR controller [17].

5.2.2 Control Scheme

The control scheme of the small dc-link drive system with active damping control is illustrated in Fig. 5.3. The "variation detection" block is used to obtain $\tilde{v}_{dc}$ and v_{dc0}. The symbol v_{dc0}, which can be obtained as $v_{dc0}=v_{dc}-\tilde{v}_{dc}$, represents the part of dc-link voltage that will not be damped by the active damping methods. While flag k_{rip} is introduced to control whether the fundamental compo-

nent of the dc-link voltage ripple $\tilde{v}_{rip1}$ will be included in $\tilde{v}_{dc}$ or not. When $k_{rip}=0$, $\tilde{v}_{rip1}$ is included in $\tilde{v}_{dc}$. When $k_{rip}=1$, $\tilde{v}_{rip1}$ is not included in $\tilde{v}_{dc}$.

Fig. 5.3. Diagram of the small dc-link drive system with active damping control.

When the gain factors g_{id}, g_{iq}, g_{vd}, g_{vq}, and g_{v0} (g_v+1) defined in (5.1), (5.5) and (5.11) are set to zero, there is no active damping control applied, and the system performance at 1500rpm 12A load (machine RMS current) condition is shown in Fig. 4.2.

5.2.3 Performance of Active Damping Methods

Fig. 5.4 shows the experimental result when $k_{rip}=0$ and $g_{vd}=1$, which means that $\tilde{v}_{rip1}$ is included in $\tilde{v}_{dc}$ and the injected voltage $\tilde{v}_d$ is equal to $\tilde{v}_{dc}$. It can be seen that compared with no active damping in Fig. 4.2, the dc-link voltage variation peak-to-peak value has reduced from about 206V to about 113V. The magnitude of the 300Hz rectified voltage component of the dc-link voltage is reduced from 49.8V to 42.6V, and the magnitude of the 600Hz oscillating voltage component is reduced from 56.5V to 21.1V. The grid current THD is reduced from 69.0% to 40.9% and the PWHD is reduced from 67.0% to 41.9% by applying active damping control. However, it should be noted that there is obvious machine current ripple as shown in Fig. 5.4 (a), when $\tilde{v}_{rip1}$ is included in $\tilde{v}_{dc}$ and being compensated. Compared with no active damping, the magnitudes of the 5th and 7th harmonics of the machine current are increased from 0.251A and 0.175A to 0.859A and 0.262A, respectively. The motor current THD is increased from 3.7% to 5.7%.

Fig. 5.5 shows the experimental result when $k_{rip}=1$ and $g_{vd}=1$, which means that $\tilde{v}_{rip1}$ is excluded from $\tilde{v}_{dc}$, so that the machine current ripple around the rectified voltage frequency (300Hz), which includes the 5th and 7th harmonics, will be greatly reduced compared with the results given in Fig. 5.4. It can be seen that the dc-link voltage variation peak-to-peak value is about 130V. The 300Hz rectified voltage component is undamped, which is 51.3V and very close to the value without active damping control. While the 600Hz oscillating voltage component is 22.8V, which is close to the result in Fig. 5.4. The THD and the PWHD values are 44.4% and 50.8% respectively, which are increased a bit compared with the condition shown in Fig. 5.4 since 300Hz rectified voltage com-

ponent is not compensated. However, the machine current THD is reduced from 5.7% to 3.9% as expected.
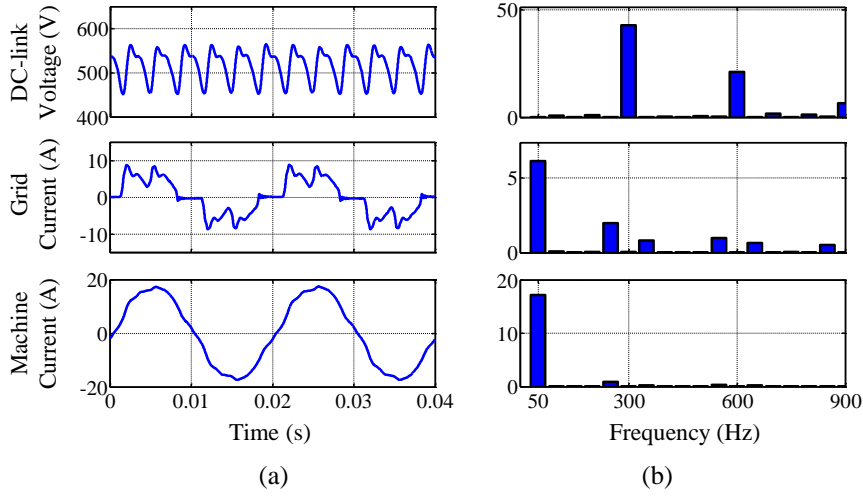

(a)　　　　　　　　　　　　　　　　(b)

Fig. 5.4. Experimental results at 1500rpm 12A load when voltage injection active damping control is applied with $k_{rip}=0$ and $g_{vd}=1$. (a) Waveforms. (b) Spectrum without dc component.
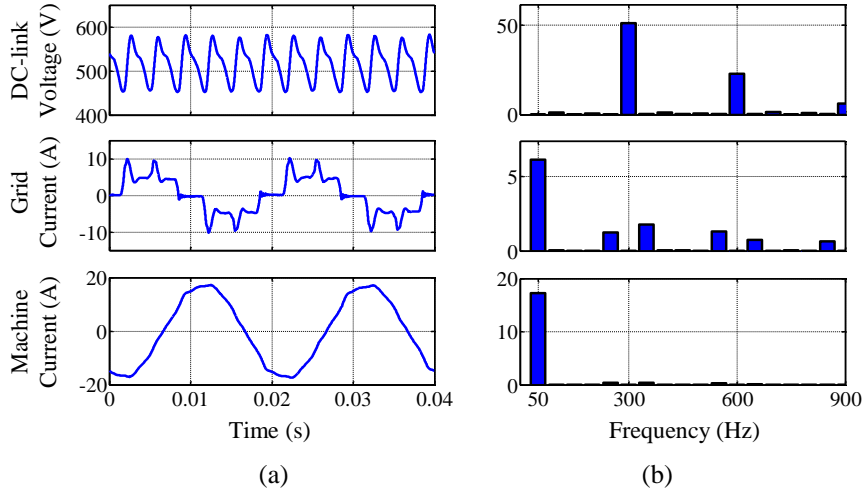

(a)　　　　　　　　　　　　　　　　(b)

Fig. 5.5. Experimental results at 1500rpm 12A load when voltage injection active damping control is applied with $k_{rip}=1$ and $g_{vd}=1$. (a) Waveforms. (b) Spectrum without dc component.

When $g_{v0}=2$ and $k_{rip}=0$, the "virtual positive impedance" method is applied with reversed $\tilde{v}_{dc}$ to reconstruct v_{dc}^{ref} and $\tilde{v}_{rip1}$ is not included in v_{dc0}, which is exactly the situation illustrated in Fig. 5.1. The experimental system performance at this situation is shown in Fig. 5.6. It can be seen that compared with no active damping, the dc-link voltage variation peak-to-peak value has reduced from about 206V to about 110V. The magnitude of the 600Hz oscillating voltage component is reduced to about 18.5V. The grid current THD is reduced from 69.0% to 38.5% and the PWHD is reduced from 67.0% to 47.4% by applying active damping control. Obvious machine current ripple can be observed, which mainly includes the 5th and 7th harmonics, since $\tilde{v}_{rip1}$ is included in $\tilde{v}_{dc}$. The motor current THD is increased from 3.7% to 10.7%.

As analyzed in the above section 5.1.3, the system can be damped when $v_{dc}^{ref}=V_{dc}$, i.e. $g_{v0}=1$ and $k_{rip}=0$. Fig. 5.7 shows the experimental results when $v_{dc}^{ref}=V_{dc}$. It can be seen that compared with undamped situation, the dc-link voltage variation peak-to-peak value is reduced to 139V. The mag-

nitude of the 600Hz oscillating voltage component is about 28.8V, which is higher than the result shown in Fig. 5.6 since the gain factor g_{v0} is reduced from two to one. The grid current THD and the PWHD values are reduced to 41.8% and 50.3% respectively. While the motor current THD is increased to 7.9%.
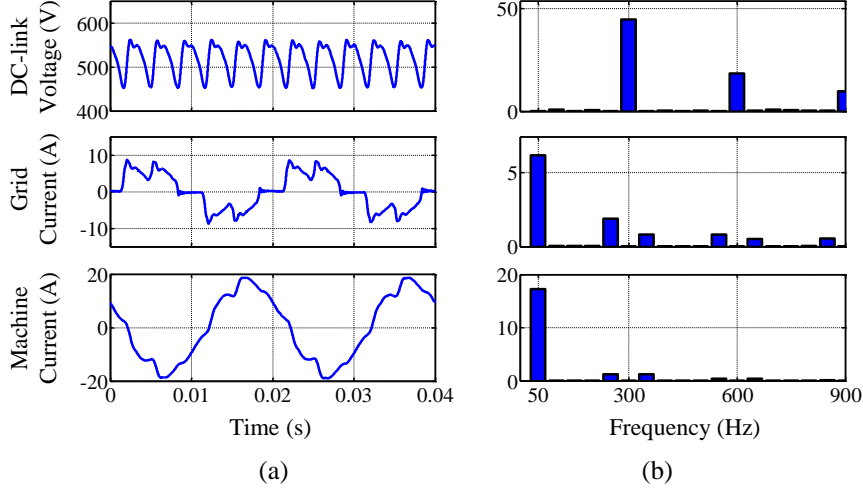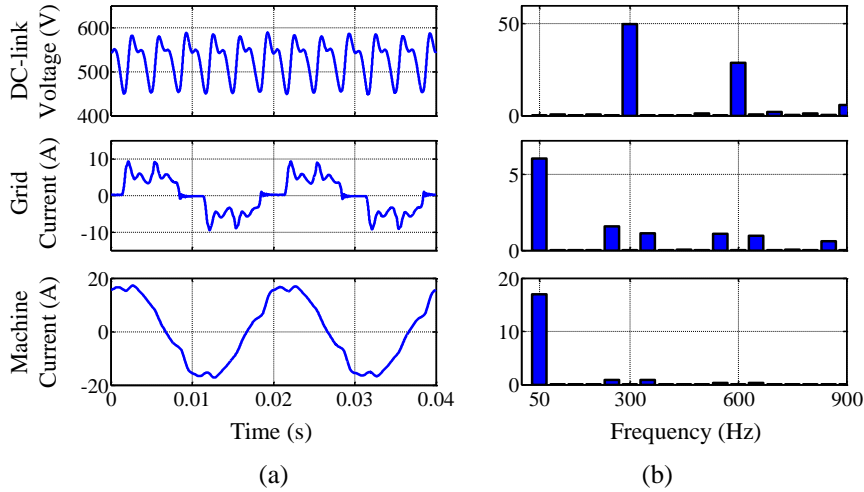

Fig. 5.6. Experimental results at 1500rpm 12A load when "virtual positive impedance" active damping control is applied with $g_{v0}=2$ and $k_{rip}=0$. (a) Waveforms. (b) Spectrum without dc component.

Fig. 5.7. Experimental results at 1500rpm 12A load when "virtual positive impedance" active damping control is applied with $v_{dc}^{ref}=V_{dc}$ (i.e. $g_{v0}=1$ and $k_{rip}=0$). (a) Waveforms. (b) Spectrum without dc component.

Fig. 5.8 shows the experimental result when $g_{v0}=2$ and $k_{rip}=1$, where $\tilde{v}_{rip1}$ is excluded from $\tilde{v}_{dc}$ to reduce the machine current ripple around the rectified voltage frequency (300Hz), i.e. the 5th and 7th harmonics. It can be seen that the dc-link voltage variation peak-to-peak value is about 116V. The magnitude of the 600Hz oscillating voltage component is about 19.3V, which is close to the result shown in Fig. 5.6 since the values of the gain factor g_{v0} are the same. The THD and the PWHD values are 39.4% and 44.6% respectively, which are increased a bit compared with the condition shown in Fig. 5.6. However, the machine current THD is reduced from 10.7% to 7.5% as expected since the 300Hz component is reduced.

Table 5.1 lists the performance of the active damping control at different control configurations when the machine is operating at 1500rpm 12A load.
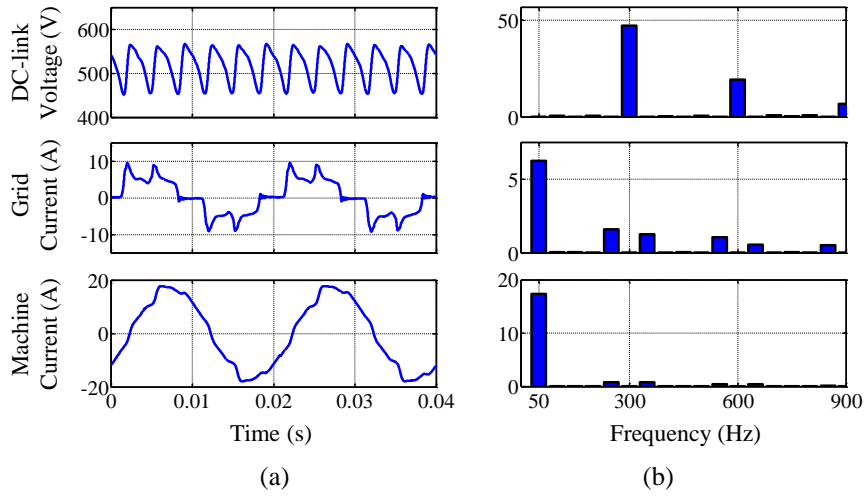
Fig. 5.8. Experimental results at 1500rpm 12A load when "virtual positive impedance" active damping control is applied with $g_{v0}=2$ and $k_{rip}=1$. (a) Waveforms. (b) Spectrum without dc component.

Table 5.1. Active Damping Control Performance at 1500rpm 12A load Condition

Control configurations	$\tilde{v}_{dc}$ [a] peak-to-peak value (V)	V_{dc300} [b] (V)	V_{dc600} [c] (V)	Grid current THD	Grid current PWHD	Machine Current THD
No active damping	206	49.8	56.5	69.0%	67.0%	3.7%
$k_{rip}=0$, $g_{vd}=1$	113	42.6	21.1	40.9%	41.9%	5.7%
$k_{rip}=0$, $g_{vq}=1$	94	38.5	14.2	37.5%	40.7%	13.7%
$k_{rip}=1$, $g_{vd}=1$	130	51.3	22.8	44.4%	50.8%	3.9%
$k_{rip}=1$, $g_{vq}=1$	118	52.2	16.3	42.4%	46.9%	5.4%
$k_{rip}=1$, $g_{vd}=0.55$	133	52.3	23.0	54.1%	50.1%	5.6%
$k_{rip}=0$, $g_{v0}=2$	110	44.5	18.5	38.5%	47.4%	10.7%
$k_{rip}=0$, $g_{v0}=1$	139	49.8	28.8	41.8%	50.3%	7.9%
$k_{rip}=1$, $g_{v0}=2$	116	47.3	19.3	39.4%	44.6%	7.5%
$k_{rip}=1$, $g_{v0}=3$	120	47.7	13.7	38.4%	40.4%	9.5%

[a] DC-link voltage variation term

[b] Amplitude of 300Hz component of $\tilde{v}_{dc}$

[c] Amplitude of 600Hz component of $\tilde{v}_{dc}$

5.2.4 Active Damping with Position Sensorless Control

Since the dc-link voltage is the only dc-link parameter used in the motor control and the dc-link voltage oscillation increases as the load increases, position-sensorless drive at rated speed and heavy load should be tested. Fig. 5.9 shows the sensorless FOC performance at 1500rpm 12A load without active damping control, which is considered to be the worst case as the variation of the dc-link voltage is maximized. It can be seen that the system can perform well with good speed and position estimation.

Fig. 5.10 and Fig. 5.11 show the system performance of sensorless FOC with different active damping controls at 1500rpm 12A load condition. It can be seen that the influence to the performance of position and speed estimation is very limited. The injection of the high frequency voltage and current caused by the active damping control methods brings very little impact to the sensorless operation performance of the drive system.
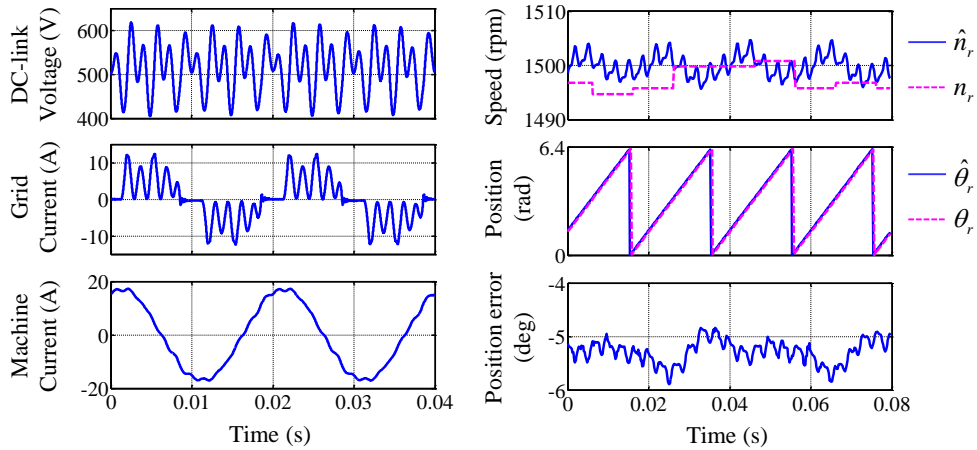
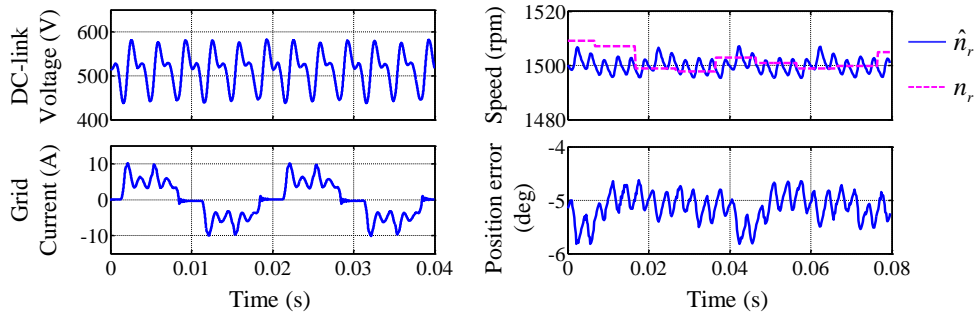Fig. 5.9. Experimental results at 1500rpm 12A load sensorless FOC without active damping controls.

Fig. 5.10. Experimental results at 1500rpm 12A load sensorless FOC with "virtual positive impedance" active damping control with $k_{rip}=0$ and $g_{v0}=2$.
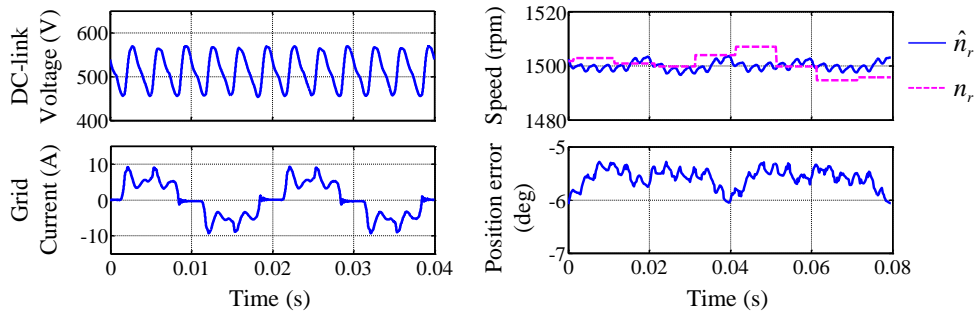

Fig. 5.11. Experimental results at 1500rpm 12A load sensorless FOC with voltage injection active damping control with $k_{rip}=1$ and $g_{vq}=1$.

Step load change at low speed is always the challenge regarding the sensorless control. In small dc-link system, the dc-link voltage variation varies as the load changes, which makes the situation even worse. Therefore, step load change at low speed is investigated. Fig. 5.12 shows the experimental sensorless FOC performance without active damping controls at 300rpm 12A step load change. It can be seen that compared with normal dc-link drive, the position error is at a similar level, which means that the performance of position-sensorless control is not sensitive to the variation of dc-link voltage caused by the small dc-link drive.

Fig. 5.13 and Fig. 5.14 show the system performance of sensorless FOC with different active damping controls at 300rpm 12A step load condition. Satisfactory results can be observed.
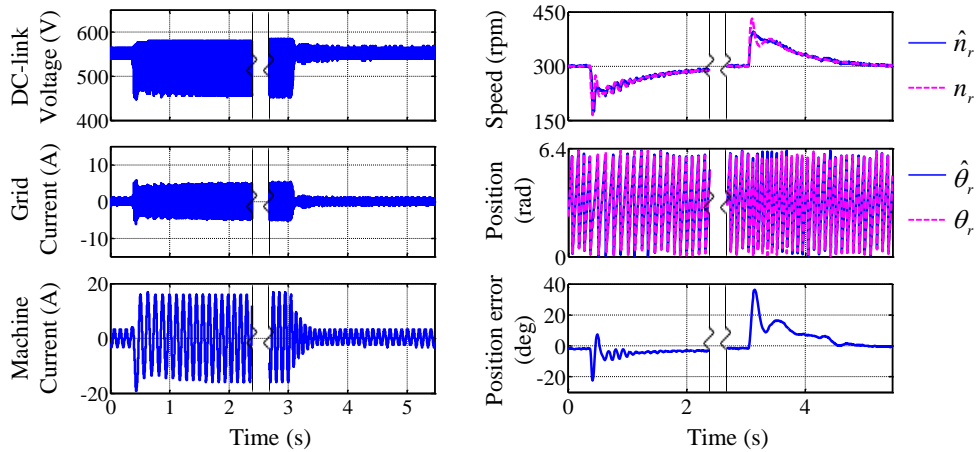
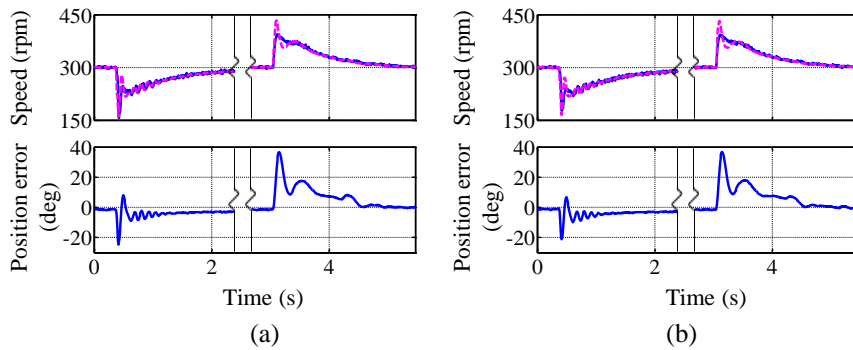Fig. 5.12. Experimental results at 300rpm 12A step load sensorless FOC without active damping controls.

(a)   (b)

Fig. 5.13. Experimental results at 300rpm 12A step load sensorless FOC with "virtual positive impedance" active damping control. (a) k_{rip}=0. (b) k_{rip}=1.

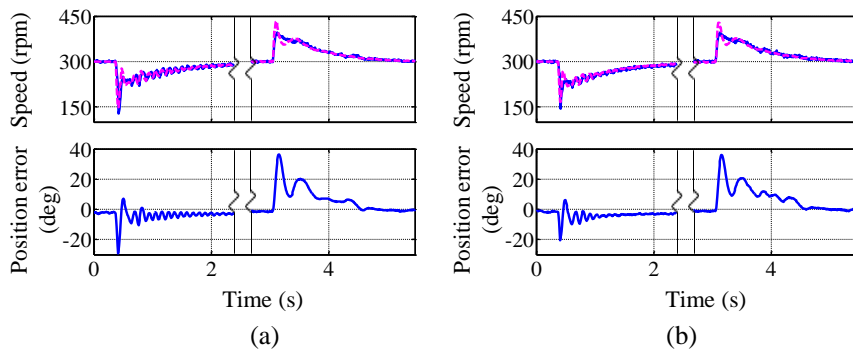

(a)   (b)

Fig. 5.14. Experimental results at 300rpm 12A step load sensorless FOC with voltage injection active damping control. (a) k_{rip}=1 and g_{vd}=1. (b) k_{rip}=1 and g_{vq}=1.

5.3 Summary

The active damping methods are analyzed and verified experimentally, and the results show that it can damp the oscillation effectively. The proposed "virtual positive impedance" active damping method can ensure the system stability without the need of obtaining the compensating gain factors dynamically according to the system parameters and operating conditions. A gain factor g_{v0} is introduced to control the deviation between the real dc-link voltage and the reference dc-link voltage

used in PWM. The system stability can be ensured when $g_{v0} \geq 1$. The damping effect increases as g_{v0} increases.

The position-sensorless small dc-link SynRM drive system has been fully examined. The experimental results show that the introduction of the small dc-link and active damping control algorithms brings very little impact to the performance of the position-sensorless drive. The influence at steady state conditions is negligible. Small impact can be observed during step load change conditions, which might be due to the phase/time delay caused by the LPF when obtaining the dc component of the dc-link voltage. Generally, the system can operate satisfactorily and is robust enough to satisfy different operation conditions.

6 CONCLUSION

A variable speed SynRM drive system has been studied and tested extensively in this project, including position sensorless control, small dc-link active damping control, and their possible interactions.

Position estimation via flux linkage is first investigated, since the focused applications are e.g. HVAC applications where high dynamic control performance during standstill to low speed operation range is not required. A commonly used closed-loop flux observer is adopted and it is found that it cannot always work properly as expected. System oscillation phenomenon can be observed. Two solutions are proposed and verified. One solution is to enhance the closed-loop observer with a PR controller, whose cutoff frequency should be adjusted according to the estimated speed. The other is to damp the oscillation by varying the PI parameters of the speed and current regulators according to the speed estimation error. The former solution can work very well during the steady-state conditions. While the latter solution is a more simple and robust solution, especially at the conditions with sudden speed changes such as step load on or off. Regarding this project, the adaptive PI solution is preferred since it can meet the project topic and scope better, i.e. a simple but robust solution.

Small dc-link drive system, in which the electrolytic dc-link capacitors are replaced with film capacitors, is obtaining more and more interests from the industrial side, since the film capacitor has much longer expected service lifetime and also has the potential to achieve a compact design of the dc-link capacitor bank at high power ratings. However, due to the well-known negative impedance characteristic of the PWM inverter with constant power load, system instability may occur and active damping control may be required.

The active damping methods based on voltage/current injection are summarized. Furthermore, a virtual positive impedance active damping method is introduced and verified. Compared with the voltage/current injection solutions, which require on-line calculation of the compensating gain factors according to the system parameters and operating conditions, this method can ensure the system stability without the knowledge of the system parameters and operating conditions. The compensating gain factor introduced in the proposed method is used to control the level of the damping effect, such as without damping, with damping, twice damping effect, etc. Thus, the compensating gain factor is a fixed user input, rather than a varying value calculated on-line which may have stability problem. Therefore, this method is much simple and robust.

Finally, the preferred flux linkage based position estimation method with adaptive PI controllers is used to cooperate with different active damping methods, so that the whole variable speed SynRM drive system can be built and tested. It is found that the whole system can perform well.

Based on the above findings, it can be concluded that the whole variable speed SynRM drive system can perform well. The solution based on the flux linkage based position estimation method with adaptive PI controllers and the virtual positive impedance active damping method is preferred and recommended so far.

6.1 Scientific Contributions

The following contributions can be highlighted:
Closed-loop flux observer analysis is carried out regarding its possible error compensation function. The limitation of this widely used closed-loop flux observer is found and solutions are proposed and verified.
Virtual positive impedance concept is introduced and analyzed for small dc-link active damping,

which can ensure the system stability without the need of obtaining the compensating gain factors dynamically according to the system parameters and operating conditions. The damping effect can be simply controlled by a damping factor.

Small dc-link position sensorless control is carried out. The influence of the active damping control to the position sensorless drive is studied. Recommendation of the active damping methods is given from the position sensorless drive point of view.

6.2 Future Work

Though many topics have been addressed and analyzed, there are still some issues that can be improved and require further studies. These issues are summarized as following:

Speed estimation Speed filter is used to provide smooth speed signal for the closed-loop feedback control. However, phase delay will be caused by the filter and the dynamic performance will be influenced at e.g. step load change conditions. Therefore, it is of great interest to improve the speed estimation by proper compensation techniques or predictive control methods.

Sampling delay compensation The sampling delay existing in the DSP system may influence the performance of the small dc-link active damping methods, especially when the resonant frequency is close to the sampling frequency. Predictive control theory may be adopted to handle such problem, since the delay is normally known and fixed. Then, it is possible to eliminate the converter dc choke/inductor in the small dc-link drive system, where the resonant frequency could be high when connected to stiff grid.

Dc-link voltage ripple prediction The dc-link oscillating voltage, which should be damped by the control methods, is generally obtained by subtracting the dc-link voltage ripple from the measured dc-link voltage. However, the dc-link voltage ripple varies for different converter input and output as well as the system parameters. Therefore, an accurate prediction of the dc-link voltage ripple will be helpful in finding the correct signal (i.e. the dc-link oscillating voltage) that should be damped, so that a better system performance can be finally obtained.

LITERATURE LIST

[1] T. Lipo, "Synchronous Reluctance Machines - A Viable Alternative for AC Drives?," in *Evolution and Modern Aspects of Synchronous Machines*, Zurich, Switzerland, Aug. 1991.

[2] D. Wang, K. Lu, and P. O. Rasmussen, "A general and intuitive approach to understand and compare the torque production capability of AC machines," in *Proc. ICEMS*, Hangzhou, China, Oct. 2014, pp. 3136–3142.

[3] "Film technology to replace electrolytic technology," AVX Co., Fountain Inn, SC, 2005. [Online]. Available: http://www.avx.com/docs/techinfo/filmtech.pdf

[4] M. Salcone and J. Bond, "Selecting film bus link capacitors for high performance inverter applications," in *Proc. IEMDC*, Miami, FL, May 2009, pp.1692–1699.

[5] P. P. Acarnley, and J.F. Watson, "Review of position-sensorless operation of brushless permanent-magnet machines," *IEEE Trans. Ind. Electron.*, vol. 53, no. 2, pp. 352–362, Apr. 2006.

[6] K. J. Meessen, P. Thelin, J. Soulard, and E. A. Lomonova, "Inductance Calculations of Permanent-Magnet Synchronous Machines Including Flux Change and Self- and Cross-Saturations," *IEEE Trans. on Magnetics,* vol. 44, no. 10, pp. 2324–2331 , Oct. 2008.

[7] P. Guglielmi, M. Pastorelli, and A. Vagati, "Impact of Cross-Saturation in Sensorless Control of Transverse-Laminated Synchronous Reluctance Motors," *IEEE Trans. Ind. Electron.,* vol. 53, no. 2, pp. 429–439, Apr. 2006.

[8] P. C. Krause, O. Wasynczuk, and S. D. Sudhoff, *Analysis of Electric Machinery and Drive System*, 2nd ed., New York: Wiley-IEEE Press, 2002, pp. 481–523.

[9] Z. Wang, K. Lu, and F. Blaabjerg, "A simple startup strategy based on current regulation for back-EMF-Based sensorless control of PMSM," *IEEE Trans. Power Electron.*, vol. 27, no. 8, pp. 3817–3825, Aug. 2012.

[10] I. Boldea, M. C. Paicu, and G. D. Andreescu, "Active flux concept for motion-sensorless unified AC drives," *IEEE Trans. Power Electron.*, vol. 23, no. 5, pp. 2612–2618, Sep. 2008.

[11] P. L. Jansen, R. D. Lorenz, and D. W. Novotny, "Observer-based direct field orientation: Analysis and comparison of alternative methods," *IEEE Trans. Ind. Appl.*, vol. 30, pp. 945–953, Jul./Aug. 1994.

[12] S. C. Agarlita, I. Boldea, and F. Blaabjerg, "High-frequency-injection -assisted "active flux"-based sensorless vector control of reluctance synchronous motors, with experiments from zero speed," *IEEE Trans. Ind. Appl.*, vol. 48, no. 6, pp. 1931–1939, Nov./Dec. 2012.

[13] T. Tuovinen, and M. Hinkkanen, "Signal-Injection-Assisted Full-Order Observer With Parameter Adaptation for Synchronous Reluctance Motor Drives," *IEEE Trans. Ind. Appl.*, vol. 50, no. 5, pp. 3392–3402, Sep./Oct. 2014.

[14] J. Holtz and J. Quan, "Sensorless vector control of induction motors at very low speed using a nonlinear inverter model and parameter identification," *IEEE Trans. Ind. Appl.*, vol. 38, no. 4, pp. 1087–1095, Jul./Aug. 2002.

[15] A. R. Munoz and T. A. Lipo, "On-line dead-time compensation technique for open-loop PWM-VSI drives," *IEEE Trans. Power Electron.*, vol. 14, no. 4, pp. 683–689, Jul. 1999.

[16] H. Zhao, Q. M. J. Wu and A. Kawamura, "An accurate approach of nonlinearity compensation for VSI inverter output voltage," *IEEE Trans. Power Electron.*, vol. 19, no. 4, pp.1029–1035, Jul. 2004.

[17] R. Teodorescu, F. Blaabjerg, M. Liserre, and P. C. Loh, "Proportional- resonant controllers and filters for grid-connected voltage-source converters," *IEE Proc. Electr. Power Appl.*, vol. 153, no. 5, pp.750–762, Sep. 2006.

[18] R. Maheshwari, S. Munk-Nielsen, and Kaiyuan Lu, "An active damping technique for small

dc-link capacitor based drive system," IEEE Trans. on Industrial Informatics, vol. 9, no. 2, pp. 848-858, May 2013.

[19] L. Mathe, H. R. Anderson, R. Lazar, and M. Ciobotaru, "DC-link compensation method for slim dc-link drives fed by soft grid," in Proc. ISIE, Bari, Italy, Jul. 2010, pp. 1236–1241.

[20] M. Hinkkanen, L. Harnefors, and J. Luomi, "Control of induction motor drives equipped with small dc-link capacitance," in Proc. EPE, Aalborg, Denmark, Sep. 2007, pp. 1–10.

[21] K. Pietilainen, L. Harnefors, A. Petersson, and H.-P. Nee, "DC-link stabilization and voltage sag ride-through of inverter drives," IEEE Trans. Ind. Electron., vol. 53, no. 4, pp. 1261–1268, Aug. 2006.

[22] D. Wang, K. Lu, P. O. Rasmussen, L. Mathe, and Y. Feng, "Analysis of Voltage Modulation Based Active Damping Techniques for Small DC-Link Drive System," in Proc. ECCE, Montreal, Canada, Sep. 2015, pp. 2927–2934.

[23] W.-J. Lee and S.-K. Sul, "DC-link voltage stabilization for reduced dc-link capacitor inverter," IEEE Trans. Ind. Appl., vol. 50, no. 1, pp. 404–414, Jan. 2014.

[24] S. D. Sudhoff, K. A. Corzine, S. F. Glover, H. J. Hegner, and H. N. Robey, "DC link stabilized field oriented control of electric propulsion systems," IEEE Trans. Energy Convers., vol. 13, no. 1, pp. 27–33, Mar. 1998.

[25] H. Mosskull, J. Galic, and B. Wahlberg, "Stabilization of induction motor drives with poorly damped input filters," IEEE Trans. Ind. Electron., vol. 54, no. 5, pp. 2724–2734, Oct. 2007.

[26] P. Magne, D. Marx, B. Nahid-Mobarakeh, and S. Pierfederici, "Large-signal stabilization of a dc-link supplying a constant power load using a virtual capacitor: Impact on the domain of attraction," IEEE Trans. Ind. Appl., vol. 48, no. 3, pp. 878–887, May/Jun. 2012.

[27] P. Liutanakul, A.-B. Awan, S. Pierfederici, B. Nahid-Mobarakeh, and F. Meibody-Tabar, "Linear stabilization of a dc bus supplying a constant power load: A general design approach," IEEE Trans. Power Electron., vol. 25, no. 2, pp.475–488, Feb. 2010.

[28] Y. A.-R. I. Mohamed, A. A. A. Radwan, and T. K. Lee, "Decoupled reference-voltage-based active dc-link stabilization for PMSM drives with tight-speed regulation," IEEE Trans. Ind. Electron., vol. 59, no. 12, pp.4523–4536, Dec. 2012.

[29] "Harmonics," Danfoss A/S, Nordborg, Denmark. [Online]. Available: http://www.danfoss.com/NR/rdonlyres/AF4DDB73-B11C-4886-B1E0-3F76C 1ACDF06/0/inst_po_garmonikam_ENG.pdf

[30] M. Cespedes, T. Beechner, L. Xing, and J. Sun, "Stabilization of constant-power loads by passive impedance damping," in Proc. APEC, Palm Springs, CA, Feb. 2010, pp. 2174–2180.

[31] H. Ertl, and J. W. Kolar, "A constant output current three-phase diode bridge rectifier employing a novel "electronic smoothing inductor"," IEEE Trans. Ind. Electron., vol. 52, no. 2, pp. 454–461, Apr. 2005.

[32] H. Shin, H.-G. Choi, and J.-I. Ha, "DC-link shunt compensator for three-phase system with small DC-link capacitor," in Proc. ICPE-ECCE Asia, Seoul, South Korea, Jun. 2015, pp. 33–39.

[33] L. Mathe, F. Iov, D. Sera, L. Torok, and R. Teodorescu, "Implementation of PLL and FLL trackers for signals with high harmonic content and low sampling frequency," in Proc. OPTIM, Bran, May 2014, pp. 633–638.